Science Advances
AAAS

Supplementary Materials for

Study of self-assembly behavior and ionic conductivity of conjugated liquid crystals with T-shaped facial-polyphilic structure

Ziwei Liu *et al.*

Corresponding author: Christopher K. Ober, cko3@cornell.edu; Paul F. Nealey, nealey@uchicago.edu; Fernando A. Escobedo, fe13@cornell.edu

Sci. Adv. **11**, eadt8303 (2025)
DOI: 10.1126/sciadv.adt8303

This PDF file includes:

S1 Materials Synthesis and Characterization

S1.1 Materials

N-bromosuccinimide (NBS), 2-hexylthiophene, 3-thiopheneethanol, 2-thiopheneboronic acid pinacol ester were purchased from AK Scientific, Inc. 2-isopropoxy-4,4,5,5-tetramethyl-1,3,2-dioxaborolane, n-butyllithium solution (1.6 M in hexane), poly(ethylene glycol) methyl ether (MW ~ 550), 1-bromodecane, tetrakis(triphenylphosphine)palladium(0) ($Pd(PPh_3)_4$) were purchased from Sigma-Aldrich. Potassium carbonate (K_2CO_3) and organic solvent such as hexane, ethyl acetate (EtOAc), tetrahydrofuran (THF), and methanol (MeOH) were purchased from Fisher. 1,2-dimethoxyethan (DME) was purchased from Honeywell. All reagents and solvents were used as received unless otherwise noted. Anhydrous THF was freshly distilled from sodium and benzophenone prior to use. NBS was recrystallized in water and stored in refrigerator before use.

S1.2 Synthetic procedures

Synthesis of EO_{n-1}-tosylate **(1)**

EO2-tosylate (n = 3) was provided by our collaborator from University of Washington. EO3-tosylate (n = 4) was synthesized according to our previous work (26). The synthetic procedure of EO9-tosylate (n ~ 10) is described here: To a 500 mL round bottom flask with a magnetic bar, poly(ethylene glycol) methyl ether (MW ~ 550, 20 mmol, 1.0 eq) dissolved in 30 mL THF was added. Sodium hydroxide (70 mmol, 3.5 eq) was dissolved in 20 mL H_2O and then added slowly to the flask. After the reaction mixture was cooled down to 0 °C in an ice bath, p-toluenesulfonyl chloride (24 mmol, 1.2 eq) dissolved in another 30 mL THF was added dropwise to the mixture under vigorous stirring. The reaction mixture was stirred at 0 ˚C for 2 h, and then at room temperature for 12 h. After completion of the reaction as indicated by TLC, the reaction mixture was poured to 5 wt% hydrochloric acid aqueous solution, and the product was extracted with dichloromethane (30 mL×3). The organic layer was then washed successively with saturated sodium bicarbonate solution (50 mL×3) and water (50 mL×3) and dried over anhydrous magnesium sulfate. After solvent evaporation, compound **1** was obtained as a slight yellow liquid without further purification, yield 70%.

^{1}H NMR (300 MHz, $CDCl_3$, δ): 7.80 (d, *J* = 9 Hz, 2H; Ar H), 7.35 (d, *J* = 9 Hz, 2H; Ar H), 4.14 (t, *J* = 4.83 Hz, 2H; CH_2), 3.63 (m, 52H, $(CH_2)_n$), 3.55 (m, 2H; CH_2), 3.37 (s, 3H; CH_3), 2.44 (s, 3H; CH_3).

^{13}C NMR ($CDCl_3$, 75 MHz, δ): 145.13, 133.27, 130.14, 128.31, 72.21, 71.06, 70.87, 69.56, 68.99, 59.39, 50.72, 31.36, 21.98.

Synthesis of 2,5-dibromo-3-thiophenemethanol / 2,5-dibromo-3-thiopheneethanol **(2)**

2-thiophenemethanol (or 2-thiopheneethanol) (20 mmol, 1.0 eq) was dissolved in 100 mL THF and cooled down to 0 °C in an ice bath. NBS (50 mmol, 2.5 eq) was added to the solution portionwise. The reaction was stirred at 0 °C for 1 h, and then at room temperature for 5 h before quenched with 10 wt% sodium hydroxide aqueous solution. The crude product was extracted with ethyl acetate (30 mL×3) and the combined organic layer washed with water (50 mL×3), then dried over $MgSO_4$. The solvent was evaporated, and the product was purified by column chromatography on silica gel with hexane: EtOAc = 5:1 (v/v) as eluent to give compound **2** as dark red liquid.

2,5-dibromo-3-thiopheneethanol (yield 83.7%), ^{1}H NMR (400 MHz, $CDCl_3$, δ): 6.87 (s, 1H; Th H), 3.82 (t, *J* = 8.60 Hz, 2H; CH_2), 2.80 (t, *J* = 8.62 Hz, 2H; CH_2).

2,5-dibromo-3-thiophenemethanol (yield 82.3%), ^{1}H NMR (400 MHz, $CDCl_3$, δ): 7.02 (s, 1H; Th H), 4.55 (d, *J* = 6.04 Hz, 2H; CH_2).

Synthesis of 2,5-dibromo-3-EO$_n$-thiophene **(3)**

To a dry round bottom flask, sodium hydride (60 wt% in mineral oil, 20 mmol, 2.0 eq) and 30 mL anhydrous THF were added. The reaction mixture was stirred under Argon atmosphere at room temperature for 30 min. Compound **2** (10 mmol, 1.0 eq) was then added dropwise via a syringe and the mixture was stirred vigorously at room temperature for 1 h. Compound **1** (12 mmol, 1.2 eq) was added to the reaction mixture slowly and stirred at room temperature overnight. After completion of the reaction as indicated by TLC, the reaction mixture was quenched with 60 mL H_2O and vigorously stirred for 30 min. The crude product was extracted with ethyl acetate (30 mL×3) and then washed with water (50 mL×3). The solvent was evaporated after dried over $MgSO_4$, and the crude product was purified by column chromatography on silica gel with hexane: EtOAc = 1:1 (v/v) as eluent to give compound **3** as a yellow liquid.

n = 3, (2,5-dibromo-3-EO3-thiophene, yield 70%), ^{1}H NMR (400 MHz, $CDCl_3$, δ): 6.99 (s, 1H; Th H), 4.60 (s, 2H; CH_2), 3.70-3.65 (m, 6H; CH_2), 3.58 (m, 2H; CH_2), 3.37 (s, 3H; CH_3).

n = 4, (2,5-dibromo-3-EO4-thiophene, yield 65%), ^{1}H NMR (400 MHz, $CDCl_3$, δ): 7.01 (s, 1H; Th H), 3.68 (m, 12H; CH_2), 3.58 (m, 2H; CH_2), 3.39 (s, 3H; CH_3), 3.00 (t, 2H; CH_2).

n ~ 10, (2,5-dibromo-3-EO10-thiophene, yield 35%), ^{1}H NMR (400 MHz, $CDCl_3$, δ): 6.98 (s, 1H; Th H), 3.63 (m, ~ 50H; CH_2), 3.54 (m, 2H; CH_2), 3.37 (s, 3H; CH_3), 3.01 (t, 2H; CH_2). ^{13}C NMR ($CDCl_3$, 75 MHz, δ): 139.58, 131.21, 111.53, 110.25, 72.21, 70.86, 67.21, 59.35.

Synthesis of 2-bromo-5-hexylthiophene **(4)**

2-hexylthiophene (40 mmol, 1.0 eq) was dissolved in 100 mL THF and cooled down to 0 °C in an ice bath. NBS (40 mmmol, 1.0 eq) was added to the solution portionwise. The reaction was stirred at 0 °C for 1 h, and then at room temperature for 5 h before quenched by 10 wt% sodium hydroxide solution. The mixture was extracted with ethyl acetate (30 mL×3), the collected organic layer was washed with water (50 mL×3), then dried over $MgSO_4$. After the solvent was evaporated via rotavap, and the crude product was purified by column chromatography on with pure hexane as eluent to give compound **4** as colorless liquid, yield 90%.

^{1}H NMR (400 MHz, $CDCl_3$, δ): 6.84 (d, J = 4 Hz, 1H; Th H), 6.53 (d, J = 4 Hz, 1H; Th H), 2.73 (t, J = 7.75 Hz, 2H; Th-C$\underline{H}_2$), 1.62 (quintet, J = 7.37 Hz, 2H; Th-CH_2-C$\underline{H}_2$), 1.30 (m, 6H; $(CH_2)_3$), 0.89 (t, J = 6.84 Hz, 3H; CH_3). ^{13}C NMR ($CDCl_3$, 75 MHz, δ): 147.98, 129.69, 124.66, 108.87, 31.86, 31.76, 30.67, 29.00, 22.90, 14.42.

Synthesis of 5-hexyl-2,2'-bithiophene **(5)**

To a 3-neck round bottom flask with a condenser, compound **4** (35 mmol, 1.0 eq), 2-thiopheneboronic acid pinacol ester (42 mmol, 1.2 eq) and K_2CO_3 (105 mmol, 3.0 eq) were added under Argon atmosphere. $Pd(PPh_3)_4$ (0.35 mmol, 0.01 eq) was added and the flask was purged Argon for 30 min. DME/H_2O mixed solvent (120 mL:30 mL, v/v) was bubbled with Argon for 40 min then transferred to the 3-neck flask via canula. The reaction mixture was refluxed at 80 °C overnight. The reaction was quenched by opening to air. The crude product was extracted with ethyl acetate (40 mL×3), then the combined organic layer was washed with water (50 mL×3) and dried over $MgSO_4$. The product was purified by column chromatography on silica gel with pure hexane as eluent to give compound **5** as a colorless liquid, yield 82%.

^{1}H NMR ($CDCl_3$, 400 MHz, δ): 7.17 (dd, J_1 = 5.12 Hz, J_2 = 1.08 Hz, 1H; Th H), 7.10 (dd, J_1 = 3.52 Hz, J_2 = 1 Hz, 1H; Th H), 7.00–6.98 (m, 2H; Th H), 6.68 (d, J = 3.56 Hz, 1H; Th H), 2.79 (t, J = 7.56 Hz, 2H; Th-Th-C$\underline{H}_2$), 1.68 (quintet, J = 7.5 Hz, 2H; Th-Th-CH_2-C$\underline{H}_2$), 1.38–1.21 (m, 6H; $(CH_2)_3$), 0.90 (t, J = 6.90 Hz, 3H; CH_3). ^{13}C NMR ($CDCl_3$, 75 MHz, δ): 145.71, 138.28, 135.04, 127.99, 125.01, 124.68, 123.70, 123.29, 31.93, 30.50, 29.11, 22.93, 14.46.

Synthesis of 5-bromo-5'-hexyl-2,2'-bithiophene **(6)**

Compound **5** (20 mmol, 1.0 eq) was dissolved in 100 mL THF and cooled down to 0 °C in an ice bath. NBS (21 mmol, 1.05 eq) was added to the solution portionwise. The reaction was stirred at 0 °C for 1 h, and then room temperature for 6 h before quenched with 10 wt% sodium hydroxide aqueous solution. The crude product was extracted with EtOAc (30 mL×3), and the combined organic layer was washed with water (50 mL×3) and dried over $MgSO_4$. The solvent was evaporated, and the crude product was purified by column chromatography on silica gel with pure hexane as eluent to give compound **6** as a white solid, yield 74%.

^{1}H NMR ($CDCl_3$, 400 MHz, δ): 6.94 (d, *J* = 4 Hz, 1H; Th H), 6.92 (d, *J* = 4 Hz, 1H; Th H), 6.83 (d, *J* = 4 Hz, 1H; Th H), 6.67 (d, *J* = 4 Hz, 1H; Th H), 2.78 (t, *J* = 8 Hz, 2H; Th-Th-C$\underline{H}_2$), 1.67 (quintet, *J* = 7.46 Hz, 2H; Th-Th-CH_2-C$\underline{H}_2$), 1.39–1.30 (m, 6H; $(CH_2)_3$), 0.89 (t, *J* = 8 Hz, 3H; CH_3). ^{13}C NMR ($CDCl_3$, 75 MHz, δ): 146.29, 136.81, 130.80, 125.11, 124.02, 123.34, 110.43, 31.89, 30.49, 29.09, 22.91, 14.44.

Synthesis of 5-(5'-(4,4,5,5-tetramethyl-1,3,2-dioxaborolan-2-yl)-5'-hexyl-2,2'-bithiophene **(7)**

To a round bottom flask, compound **6** (10 mmol, 1.0 eq) and 2-isopropoxy-4,4,5,5-tetramethyl-1,3,2-dioxaborolane (20 mmol, 2.0 eq) were dissolved in anhydrous THF (50mL). The solution was purged Argon for 30 min before cooling down to -78 °C in a dry ice/acetone bath. N-butyllithium solution (12 mmol, 1.2 eq) was added dropwise via a syringe under vigorous stirring. The reaction mixture was stirred at -78 °C for 30 min then room temperature for overnight. 10% HCl was used to quench the reaction, and crude product was extracted with ethyl acetate (30 mL×3), washed with pure water (50 mL×3) and then dried over $MgSO_4$. Column chromatography was used to purify the product with hexane/ethyl acetate (20:1, v/v) as eluent to give compound **7** as a blue liquid, yield 52%.

^{1}H NMR ($CDCl_3$, 400 MHz, δ): 7.50 (d, *J* = 4 Hz, 1H; Th H), 7.16 (d, *J* = 4 Hz, 1H; Th H), 7.04 (d, *J* = 3.56 Hz, 1H; Th H), 6.68 (d, *J* = 4 Hz, 1H; Th H), 2.78 (t, *J* = 7.76 Hz, 2H; Th-C$\underline{H}_2$), 1.67 (quintet, *J* = 8 Hz, 2H; Th-CH_2-C$\underline{H}_2$), 1.34 (s, 12H; $(CH_3)_4$), 1.32–1.28 (m, 6H; $(CH_2)_3$), 0.88 (t, *J* = 8 Hz, 3H; CH_2-C$\underline{H}_3$)

Synthesis of 5T/dC6/EOn

To a 3-neck round bottom flask, compound **7** (4.48 mmol, 2.8 eq), compound **3** (1.6 mmol, 1.0 eq) and K_2CO_3 (9.6 mmol, 6.0 eq) were added. The flask was purged with Argon for 30 min before

$Pd(PPh_3)_4$ (0.032 mmol, 0.02 eq) was added. The flask was purged with Argon for another 30 min. A mixed solvent of DME/H_2O (40 mL/10 mL, v/v) was purged with Argon for 1 h before canula transferred to the 3-neck flask. The reaction was refluxed at 80 °C overnight. The crude product was extracted with ethyl acetate (30 mL×3) and the combined organic layer was washed with pure water (30 mL×3) and then dried over $MgSO_4$. Column chromatography was used to purify the product with hexane/ethyl acetate (3:1, v/v) as eluent to give the final product as a yellow solid (for 5T/dC6/EO3 and 5T/dC6/EO4) after precipitated with methanol, filtered and dried in vacuum oven or dark red liquid (for 5T/dC6/EO10).

5T/dC6/EO3, yield 10%, ^{1}H NMR ($CDCl_3$, 400 MHz, δ): 7.18 (s, 1H; Th H), 7.11 (d, *J* = 4 Hz, 1H; Th H), 7.05 (t, *J* = 3.32 Hz, 2H; Th H), 7.00 (q, *J* = 4 Hz, 3H; Th H), 6.69 (m, 2H; Th H), 4.61 (s, 2H; Th-C$\underline{H}_2$), 3.72 (m, 4H; Th-CH_2O-(C$\underline{H}_2$)$_2$), 3.68–3.66 (m, 2H; Th-CH_2O-$(CH_2)_2$O-C$\underline{H}_2$), 3.58–3.55 (m, 2H; Th-CH_2O-$(CH_2)_2$O-CH_2-C$\underline{H}_2$), 3.38 (s, 3H; Th-CH_2O-$(CH_2)_2$O-$(CH_2)_2$O-C$\underline{H}_3$), 2.79 (t, *J* = 8 Hz, 4H; 2(Th-C$\underline{H}_2$)), 1.68 (quintet, *J* = 8 Hz, 4H; 2(Th-CH_2-C$\underline{H}_2$)), 1.38–1.31 (m, 12H; 2(CH_2-CH_2-CH_2)), 0.90 (t, *J* = 8 Hz, 6H; 2(CH_3)). ^{13}C NMR ($CDCl_3$, 75 MHz, δ): 145.85, 145.75, 137.08, 132.82, 127.17, 126.34, 124.87, 124.34, 123.58, 123.54, 123.44, 70.60, 70.01, 69.52, 66.95, 65.68, 63.52, 31.56, 30.20, 28.75, 22.58, 14.10.

5T/dC6/EO4, yield 12%, ^{1}H NMR ($CDCl_3$, 400 MHz, δ): 7.04 (m, 4H; Th H), 6.98 (m, 3H; Th H), 6.68 (m, 2H; Th H), 3.74 (t, *J* = 6.92 Hz, 2H; CH_2), 3.66–3.60 (m, 10H; CH_2), 3.52 (m, 2H; CH_2), 3.35 (s, 3H; CH_3), 3.05 (t, *J* = 7.04 Hz, 2H; CH_2), 2.79 (t, *J* = 7.24 Hz, 4H; 2(Th-C$\underline{H}_2$)); 1.68 (quintet, *J* = 7.71 Hz, 4H; 2(Th-CH_2-C$\underline{H}_2$)), 1.31 (m, 12H; 2(CH_2-CH_2-CH_2)), 0.90 (t, *J* = 6.4 Hz, 6H; 2CH_3). ^{13}C NMR ($CDCl_3$, 100 MHz, δ): 145.77, 130.27, 129.93, 128.01, 126.63, 125.49, 124.87, 124.22, 123.71, 123.33, 71.47, 70.64, 67.49, 66.83, 59.87, 31.57, 30.20, 28.76, 22.58, 14.10.

5T/dC6/EO10, yield 10%, ^{1}H NMR ($CDCl_3$, 400 MHz, δ): 7.17 (s, 1H; Th H), 7.10 (m, 1H; Th H), 7.05–7.03 (m, 2H; Th H), 6.99 (m, 3H; Th H), 6.68 (m, 2H; Th H), 3.70–3.63 (m, 58H; CH_2), 3.37 (s, 3H; CH_3), 2.79 (t, *J* = 7.66 Hz, 4H; 2(Th-C$\underline{H}_2$)), 1.66 (quintet, *J* = 7.24 Hz, 4H; 2(Th-CH_2-C$\underline{H}_2$)), 1.33 (m, 12H; CH_2), 0.89 (t, *J* = 6.40 Hz, 6H; 2CH_3). ^{13}C NMR ($CDCl_3$, 100 MHz, δ): 125.76, 125.54, 124.87, 124.76, 123.61, 72.20, 70.55, 31.55, 30.19, 28.74, 22.56, 14.08.

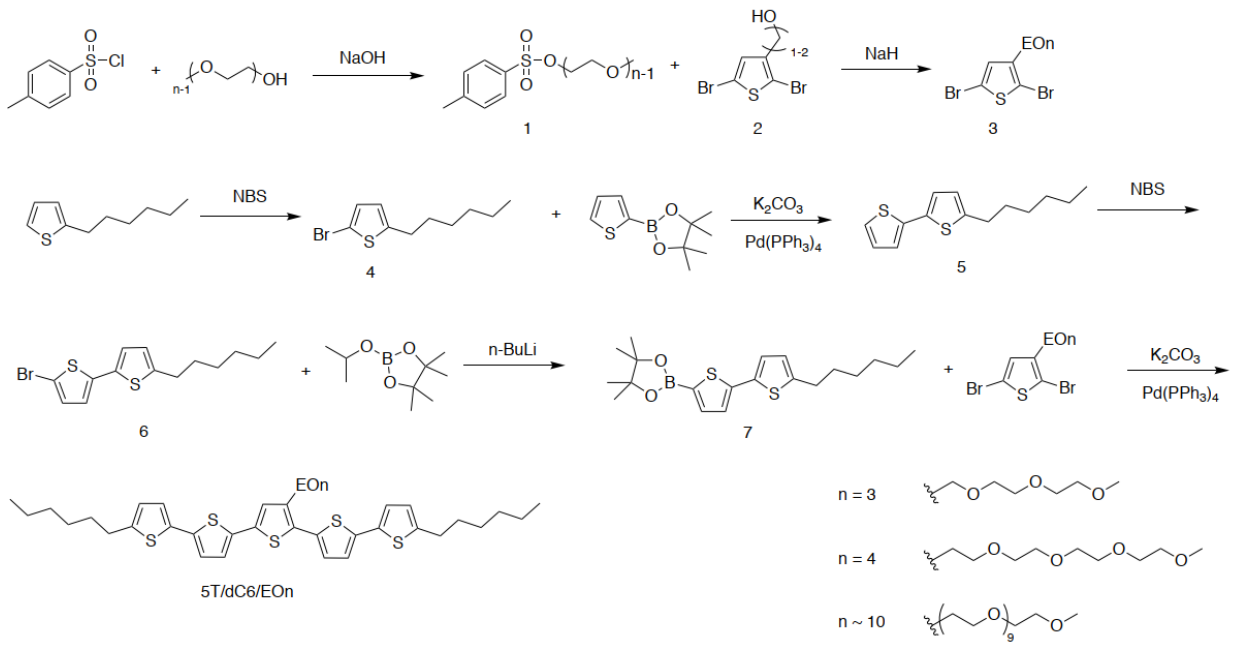

Fig. S1. Synthetic procedures of T-shaped conjugated LCs 5T/dC6/EOn.

S1.3 Characterization methods

Temperature-Dependent Wide-Angle X-ray Scattering. T-WAXS experiments were performed with SAXSLAB (XENOCS)'s GANESHA equipped with a T-95 Linkam stage at the University of Chicago X-ray facility. LC material was dissolved in THF, and the solution was pipetted into a capillary. The solvent was then evaporated, and samples were measured in transmission mode of WAXS as a function of temperature. The experiment was performed in high vacuum ($<10^{-1}$ Torr) to minimize damages to the sample and prevent extraneous scattering from air. T-dependent WAXS measurements were performed at the ramping rate of 10K/min, which was similar to the DSC measurement. Upon reaching the specific temperature the samples were allowed to equilibrate for 5-10 min prior to X-ray exposure. The exposure time for each measurement was 60-100s, and at each temperature the measurement was performed several times to ensure that the sample had reached equilibrium. The diffraction intensity of the samples at each temperature was extracted as a function of wave vector ***q*** using the SAXSGUI MATLAB program developed by SAXSLAB. Appropriate background subtraction was performed prior to comparing peak intensity at each temperature.

Grazing-Incidence Wide-Angle X-Ray Scattering. GIWAXS were performed at beamline 8-ID-E of the Advanced Photon Source, Argonne National Laboratory with 10.86 keV (λ = 1.1416 Å)

synchrotron radiation. Samples were measured inside a low vacuum chamber (10^{-3} mbar) to minimize concerns about radiation damages, samples' moisture uptake, and extraneous scattering from ambient air. For each sample, three data sets were taken from three adjacent spots on the sample and then summed to enhance the signal-to-noise ratio. The samples were tilted at an angle of incidence of 0.14° with respect to the incoming beam, which is above the estimated critical angle of sample (≈ 0.13°) but below the critical angle of the Si substrates (≈ 0.17°) to probe the whole film thickness. The scattering signal was recorded with a Pilatus 1MF pixel array detector (pixel size = 172 μm) positioned 228 mm from the sample. Each data set was stored as a 981×1043 32-bit tiff image with 20-bit dynamic range. The Pilatus detector has rows of inactive pixels at the border between detector modules. To fill these gaps, after each measurement the detector was moved to a new vertical direction and the measurement on each spot was repeated, then the gaps were filled by combining the data from two detector positions. The signals were reshaped and output as intensity maps in q_r vs. q_z space. We also performed detector nonuniformity, detection efficiency, the polarization effect, and solid-angle variation for each image. All the GIWAXS data processing and extraction were executed using the GIXSGUI package for MATLAB (66).

Peak shape analysis of GIWAXS patterns was performed on wedge cuts taken with an angular breadth of 2°. Each wedge cut was first fit to an empirical baseline function to enable the subtraction of the background intensity and amorphous scattering. The background-subtracted wedge cut was then fit to a Voigt function to extract the peak position and the FWHM of the reflections of interest. More details of peak shape analysis can be found elsewhere (67).

S1.4 Thermal behavior of 5T/dC6/EOn

Table S1. Thermal properties of 5T/dC6/EOn.

system	1st cooling	2nd heating
5T/dC6/EO3	Iso 31 ºC (29.61 kJ/mol or 41.52 J/g) Sm	Sm 48 ºC Iso
5T/dC6/EO4	Iso 20 ºC (28.67 kJ/mol or 37.18 J/g) Sm	Sm 35 ºC Iso
5T/dC6/EO10	Iso -36 ºC (32.01 J/g) Col	Col 4 ºC Iso

Note: transition temperatures (°C) are given as the maximum of the peaks detected by DSC measurements on the 1st cooling and 2nd heating at a scanning rate of 10 °C/min. The transition enthalpies are in parentheses. Sm stands for smectic phase, Col for columnar phase, and Iso for isotropic liquid.

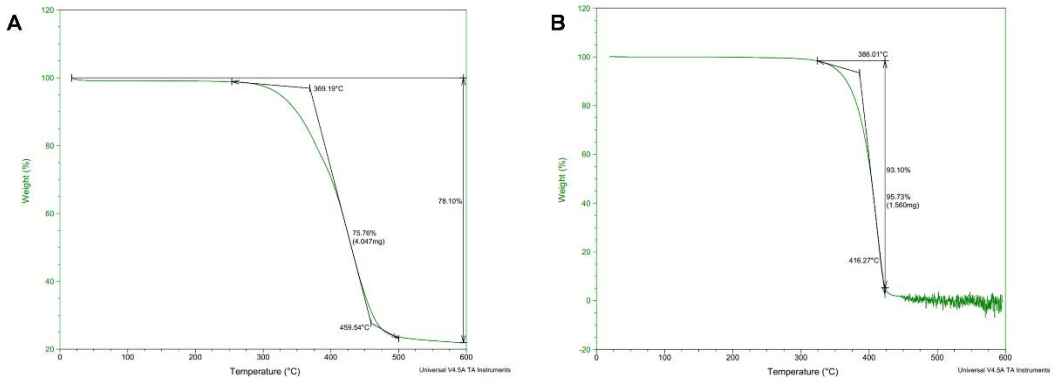

Fig. S2. Thermogravimetric analysis (TGA) of neat 5T/dC6/EOn molecules. (A) 5T/dC6/EO3, and (B) 5T/dC6/EO4. Decomposition takes place at 369.19 °C and 386.01 °C, respectively.

S2 Computational modeling and molecular dynamics (MD) simulation

A coarse-grained (CG) model and an all-atom (AA) model of 5T/dC6/EOn were used to simulate the molecular self-assembly and the Li-ion transport, respectively. LAMMPS simulation package (60, 61) with GPU acceleration (62, 63) was used to run MD simulations, and VMD (64) was used for visualizations.

S2.1 All-atom force field parameter

For the AA representation of 5T/dC6/EOn, 5T is modeled based on Misra's work (26) with modified partial charges and bonded parameters following the similar procedure, and the alkyl and oligo(ethylene oxide) (EOn) segments are modeled using the OPLS-AA force field (59). Also, the Li-ion is modeled by the OPLS-AA force field. To introduce the AA force field, different atom types are illustrated in **Fig. S3** with their relative positions within the molecule. Each atom type is represented by a combination of the chemical element symbol and a unique letter for differentiation, and each atom is represented by its type and ID. For example, "C_{A2}" stands for the carbon atom of *atomType*=CA and *atomID*=2. For clarity, we omit most of the hydrogen atoms, though the full list of atoms can be found in **Table S2–S4** with their partial charges. The rule of thumb to learn the position of hydrogen atom is the following: the *atomID* of each hydrogen atom follows right after the atom it attached. For example, "H_{A3}" attaches to "C_{A2}", "H_{C36}" and "H_{C37}" attach to "C_{T35}".

Nonbonded potentials are described by the sum of the LJ potentials for the van de Walls interactions and the Coulombic potentials for the electrostatic interactions with parameters listed in **Table S5**,

$$U_{\mathrm{AA-NB}} = 4\epsilon_{ij}\left[\left(\frac{\sigma_{ij}}{r_{ij}}\right)^{12} - \left(\frac{\sigma_{ij}}{r_{ij}}\right)^{6}\right] + \frac{q_i q_j}{4\pi\varepsilon_0 r_{ij}} \quad \text{(S1)}$$

where r_{ij} is the distance between atom i and j, σ_{ij} is the van de Walls diameter and ϵ_{ij} is the well-depth parameter both defined by the atom types, q_i and q_j are partial charges of atom i and j, ε_0 is the vacuum permittivity. The geometric mixing rules are used for the cross terms of LJ potentials,

$$\sigma_{ij} = \sqrt{\sigma_{ii}\sigma_{jj}} \quad , \quad \epsilon_{ij} = \sqrt{\epsilon_{ii}\epsilon_{jj}} \quad \text{(S2)}$$

Bonded interactions usually include the bond stretching interactions (1-2 interaction for atoms separated by one chemical bond), the angle bending interactions (1-3 interaction for atoms separated by two bonds) and the torsional rotation interactions (1-4 interaction for atoms separated by three bonds). The bond stretching and angle bending interactions are described by the harmonic form with parameters listed in **Tables S6 and S7**,

$$U_{\text{bond}} = K_b(r - r_0)^2 \quad \text{(S3)}$$

$$U_{\text{angle}} = K_\theta(\theta - \theta_0)^2 \quad \text{(S4)}$$

where K_b is the bond spring constant, r_0 is the equilibrium bond distance, r is the separation distance between two bonded atoms, K_θ is the angle spring constant, θ_0 is the equilibrium angle value, and θ is the bending angle formed by three consecutive bonded atoms. Torsional potentials are described by the following two function forms,

$$U_{\text{tors-OPLS}} = \sum_{n=1}^{3} \frac{1}{2} K_n[1 + (-1)^{n+1} \cos(n\phi)] \quad \text{(S5)}$$

$$U_{\text{tors-MultiHarmonic}} = \sum_{n=0}^{4} C_n \cos^n \phi \quad \text{(S6)}$$

where K_n and C_n are constant coefficients, ϕ is the dihedral angle formed by four consecutive bonded atoms. Only the torsional potentials with non-zero parameters are listed in **Table S8 and S9**. In addition, LJ and Coulombic potentials are turned off for atoms separated by one and two bonds, and computed with the strength scaled to 0.5 for atoms separated by three bonds. The LJ potentials are truncated at 12 Å with the tail-correction. The Coulombic potentials are calculated using the particle-particle particle-mesh method with a real-space cutoff of 10 Å and a tolerance of 10^{-4}.

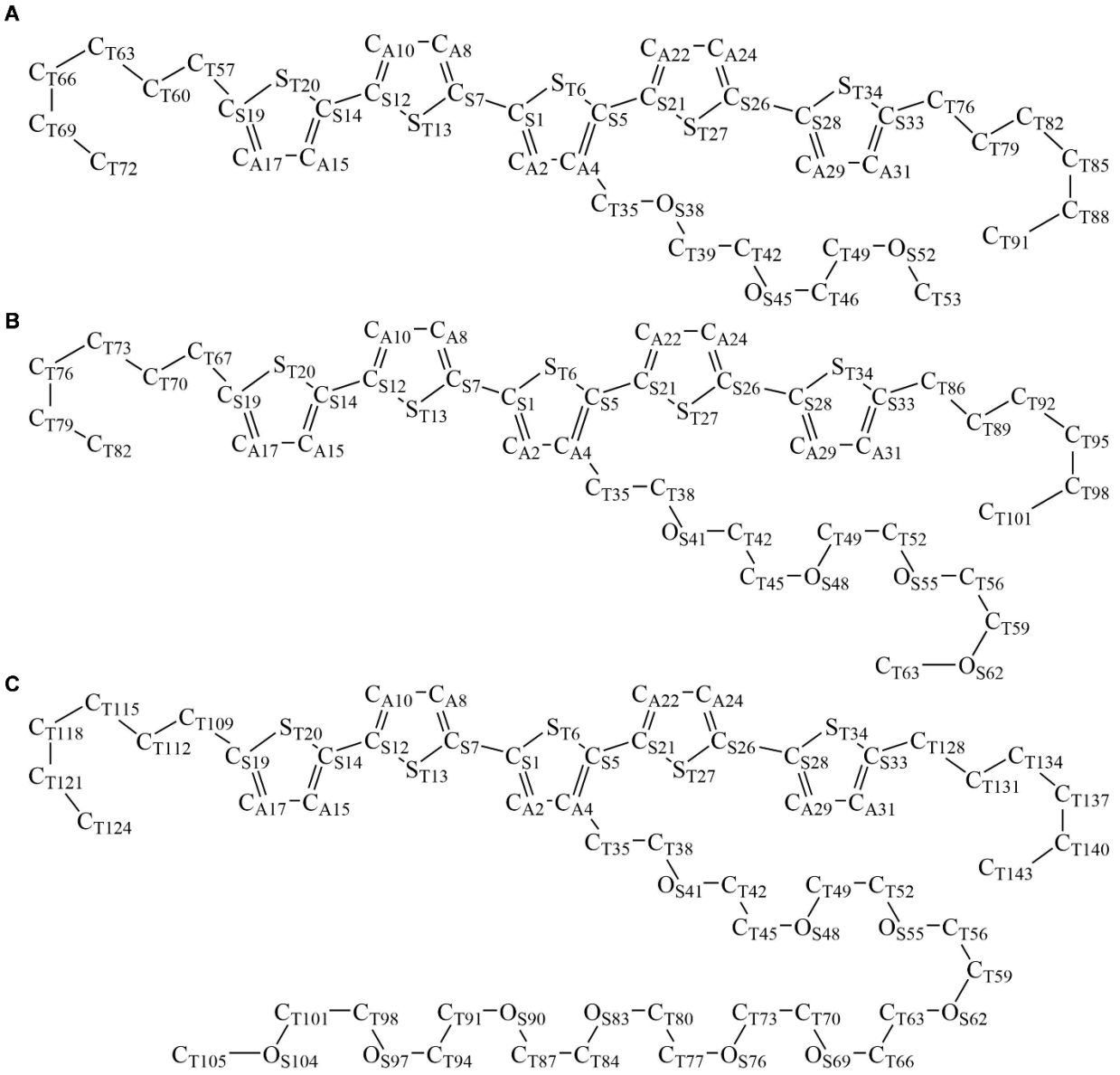

Fig. S3. Reference labels for atom types in the AA force field for 5T/dC6/EOn molecules. (A) 5T/dC6/EO3, (B) 5T/dC6/EO4 and (C) 5T/dC6/EO10. Atoms of different types in our AA model are labeled with different letter subscripts. Each atom is also labeled with a numerical subscript to indicate its *atomID*. Note that the numerical subscript is not consecutive, and missing numbers represent omitted hydrogen atoms for clarity.

Table S2. Full list of atoms in 5T/dC6/EO3 and Li-ion with partial charges.

ID	atom	q / e	ID	atom	q / e	ID	atom	q / e	ID	atom	q / e
1	CS	0.100	25	HA	0.150	49	CT	0.14	73	HC	0.06
2	CA	-0.210	26	CS	0.100	50	HC	0.03	74	HC	0.06
3	HA	0.180	27	ST	-0.120	51	HC	0.03	75	HC	0.06
4	CA	-0.210	28	CS	-0.112	52	OS	-0.40	76	CT	0.05
5	CS	0.100	29	CA	-0.280	53	CT	0.11	77	HC	0.06
6	ST	-0.120	30	HA	0.170	54	HC	0.03	78	HC	0.06
7	CS	0.080	31	CA	-0.022	55	HC	0.03	79	CT	-0.12
8	CA	-0.210	32	HA	0.137	56	HC	0.03	80	HC	0.06
9	HA	0.180	33	CS	-0.050	57	CT	0.05	81	HC	0.06
10	CA	-0.170	34	ST	-0.023	58	HC	0.06	82	CT	-0.12
11	HA	0.150	35	CT	0.30	59	HC	0.06	83	HC	0.06
12	CS	0.100	36	HC	0.03	60	CT	-0.12	84	HC	0.06
13	ST	-0.120	37	HC	0.03	61	HC	0.06	85	CT	-0.12
14	CS	-0.112	38	OS	-0.40	62	HC	0.06	86	HC	0.06
15	CA	-0.280	39	CT	0.14	63	CT	-0.12	87	HC	0.06
16	HA	0.170	40	HC	0.03	64	HC	0.06	88	CT	-0.12
17	CA	-0.022	41	HC	0.03	65	HC	0.06	89	HC	0.06
18	HA	0.137	42	CT	0.14	66	CT	-0.12	90	HC	0.06
19	CS	-0.050	43	HC	0.03	67	HC	0.06	91	CT	-0.18
20	ST	-0.023	44	HC	0.03	68	HC	0.06	92	HC	0.06
21	CS	0.080	45	OS	-0.40	69	CT	-0.12	93	HC	0.06
22	CA	-0.210	46	CT	0.14	70	HC	0.06	94	HC	0.06
23	HA	0.180	47	HC	0.03	71	HC	0.06			
24	CA	-0.170	48	HC	0.03	72	CT	-0.18			
1	Li	1.0									

Table S3. Full list of atoms in 5T/dC6/EO4 with partial charges.

ID	atom	*q* / e	ID	atom	*q* / e	ID	atom	*q* / e	ID	atom	*q* / e
1	CS	0.100	27	ST	-0.120	53	HC	0.03	79	CT	-0.12
2	CA	-0.210	28	CS	-0.112	54	HC	0.03	80	HC	0.06
3	HA	0.180	29	CA	-0.280	55	OS	-0.40	81	HC	0.06
4	CA	-0.210	30	HA	0.170	56	CT	0.14	82	CT	-0.18
5	CS	0.100	31	CA	-0.022	57	HC	0.03	83	HC	0.06
6	ST	-0.120	32	HA	0.137	58	HC	0.03	84	HC	0.06
7	CS	0.080	33	CS	-0.050	59	CT	0.14	85	HC	0.06
8	CA	-0.210	34	ST	-0.023	60	HC	0.03	86	CT	0.05
9	HA	0.180	35	CT	0.04	61	HC	0.03	87	HC	0.06
10	CA	-0.170	36	HC	0.06	62	OS	-0.40	88	HC	0.06
11	HA	0.150	37	HC	0.06	63	CT	0.11	89	CT	-0.12
12	CS	0.100	38	CT	0.14	64	HC	0.03	90	HC	0.06
13	ST	-0.120	39	HC	0.03	65	HC	0.03	91	HC	0.06
14	CS	-0.112	40	HC	0.03	66	HC	0.03	92	CT	-0.12
15	CA	-0.280	41	OS	-0.40	67	CT	0.05	93	HC	0.06
16	HA	0.170	42	CT	0.14	68	HC	0.06	94	HC	0.06
17	CA	-0.022	43	HC	0.03	69	HC	0.06	95	CT	-0.12
18	HA	0.137	44	HC	0.03	70	CT	-0.12	96	HC	0.06
19	CS	-0.050	45	CT	0.14	71	HC	0.06	97	HC	0.06
20	ST	-0.023	46	HC	0.03	72	HC	0.06	98	CT	-0.12
21	CS	0.080	47	HC	0.03	73	CT	-0.12	99	HC	0.06
22	CA	-0.210	48	OS	-0.40	74	HC	0.06	100	HC	0.06
23	HA	0.180	49	CT	0.14	75	HC	0.06	101	CT	-0.18
24	CA	-0.170	50	HC	0.03	76	CT	-0.12	102	HC	0.06
25	HA	0.150	51	HC	0.03	77	HC	0.06	103	HC	0.06
26	CS	0.100	52	CT	0.14	78	HC	0.06	104	HC	0.06

Table S4. Full list of atoms in 5T/dC6/EO10 with partial charges.

ID	atom	q / e	ID	atom	q / e	ID	atom	q / e	ID	atom	q / e
1	CS	0.100	38	CT	0.14	75	HC	0.03	112	CT	-0.12
2	CA	-0.210	39	HC	0.03	76	OS	-0.40	113	HC	0.06
3	HA	0.180	40	HC	0.03	77	CT	0.14	114	HC	0.06
4	CA	-0.210	41	OS	-0.40	78	HC	0.03	115	CT	-0.12
5	CS	0.100	42	CT	0.14	79	HC	0.03	116	HC	0.06
6	ST	-0.120	43	HC	0.03	80	CT	0.14	117	HC	0.06
7	CS	0.080	44	HC	0.03	81	HC	0.03	118	CT	-0.12
8	CA	-0.210	45	CT	0.14	82	HC	0.03	119	HC	0.06
9	HA	0.180	46	HC	0.03	83	OS	-0.40	120	HC	0.06
10	CA	-0.170	47	HC	0.03	84	CT	0.14	121	CT	-0.12
11	HA	0.150	48	OS	-0.40	85	HC	0.03	122	HC	0.06
12	CS	0.100	49	CT	0.14	86	HC	0.03	123	HC	0.06
13	ST	-0.120	50	HC	0.03	87	CT	0.14	124	CT	-0.18
14	CS	-0.112	51	HC	0.03	88	HC	0.03	125	HC	0.06
15	CA	-0.280	52	CT	0.14	89	HC	0.03	126	HC	0.06
16	HA	0.170	53	HC	0.03	90	OS	-0.40	127	HC	0.06
17	CA	-0.022	54	HC	0.03	91	CT	0.14	128	CT	0.05
18	HA	0.137	55	OS	-0.40	92	HC	0.03	129	HC	0.06
19	CS	-0.050	56	CT	0.14	93	HC	0.03	130	HC	0.06
20	ST	-0.023	57	HC	0.03	94	CT	0.14	131	CT	-0.12
21	CS	0.080	58	HC	0.03	95	HC	0.03	132	HC	0.06
22	CA	-0.210	59	CT	0.14	96	HC	0.03	133	HC	0.06
23	HA	0.180	60	HC	0.03	97	OS	-0.40	134	CT	-0.12
24	CA	-0.170	61	HC	0.03	98	CT	0.14	135	HC	0.06
25	HA	0.150	62	OS	-0.40	99	HC	0.03	136	HC	0.06
26	CS	0.100	63	CT	0.14	100	HC	0.03	137	CT	-0.12
27	ST	-0.120	64	HC	0.03	101	CT	0.14	138	HC	0.06
28	CS	-0.112	65	HC	0.03	102	HC	0.03	139	HC	0.06
29	CA	-0.280	66	CT	0.14	103	HC	0.03	140	CT	-0.12
30	HA	0.170	67	HC	0.03	104	OS	-0.40	141	HC	0.06
31	CA	-0.022	68	HC	0.03	105	CT	0.11	142	HC	0.06
32	HA	0.137	69	OS	-0.40	106	HC	0.03	143	CT	-0.18
33	CS	-0.050	70	CT	0.14	107	HC	0.03	144	HC	0.06
34	ST	-0.023	71	HC	0.03	108	HC	0.03	145	HC	0.06
35	CT	0.04	72	HC	0.03	109	CT	0.05	146	HC	0.06
36	HC	0.06	73	CT	0.14	110	HC	0.06			
37	HC	0.06	74	HC	0.03	111	HC	0.06			

Table S5. Nonbonded potential parameters for 5T/dC6/EOn.

atom	m / (g/mol)	σ_{ii} / Å	ϵ_{ii} / (kcal/mol)	atom	m / (g/mol)	σ_{ii} / Å	ϵ_{ii} / (kcal/mol)
CS	12.011	3.55	0.070	CT	12.011	3.50	0.066
CA	12.011	3.55	0.070	HC	1.008	2.50	0.030
HA	1.008	2.42	0.030	OS	15.999	2.90	0.140
ST	32.060	3.55	0.250	Li	6.941	2.87	0.0005

Table S6. Harmonic bond stretching potential parameters for 5T/dC6/EOn.

bond	K_b / (kcal·mol^{-1}·Å^{-2})	r_0 / Å	bond	K_b / (kcal·mol^{-1}·Å^{-2})	r_0 / Å
CA-CS	456.892	1.374	CA-CT	317.000	1.501
CA-HA	307.105	1.084	CT-HC	340.000	1.090
CA-CA	392.459	1.433	CT-OS	320.000	1.410
CS-ST	209.200	1.734	CT-CT	268.000	1.529
CS-CS	322.168	1.450	CS-CT	265.260	1.501

Table S7. Harmonic angle bending potential parameters for 5T/dC6/EOn.

angle	K_θ / (kcal·mol^{-1}·rad^{-2})	θ_0 / °	angle	K_θ / (kcal·mol^{-1}·rad^{-2})	θ_0 / °
CA-CS-ST	58.576	111.588	CA-CT-HC	37.500	110.700
CA-CS-CS	52.718	128.421	CA-CT-OS	58.350	112.700
CS-CS-ST	52.718	120.381	HC-CT-HC	33.000	107.800
CS-CA-HA	29.288	123.496	HC-CT-OS	35.000	109.500
CA-CA-CS	58.576	113.625	CT-OS-CT	60.000	109.500
CA-CA-HA	29.288	122.873	CT-CT-OS	50.000	109.500
CA-CA-CT	70.000	122.763	CT-CT-HC	37.500	110.700
CS-CA-CT	70.000	125.380	CS-CT-HC	37.500	110.700
CS-ST-CS	61.923	91.739	CS-CT-CT	58.350	112.700
CA-CS-CT	29.288	123.496	CT-CT-CT	58.350	112.700
CT-CS-ST	29.288	120.366	CA-CT-CT	58.350	112.700

Table S8. OPLS torsional potential parameters for 5T/dC6/EOn. K_n: kcal·mol^{-1}.

torsion	K_1	K_2	K_3	torsion	K_1	K_2	K_3
CA-CT-OS-CT	0.650	-0.250	0.670	HC-CT-CT-HC	0.000	0.000	0.300
HC-CT-OS-CT	0.000	0.000	0.760	CS-CT-CT-HC	0.000	0.000	0.366
CT-CT-OS-CT	0.650	-0.250	0.670	CS-CT-CT-CT	2.732	-0.229	0.485
HC-CT-CT-OS	0.000	0.000	0.468	CT-CT-CT-HC	0.000	0.000	0.300
OS-CT-CT-OS	-0.550	0.000	0.000	CT-CT-CT-CT	1.300	-0.050	0.200
CA-CT-CT-HC	0.000	0.000	0.366	CA-CT-CT-OS	2.732	-0.229	0.485

Table S9. Multi-harmonic torsional potential parameters for 5T/dC6/EOn. K_n: kcal·mol^{-1}.

torsion	K_0	K_1	K_2	K_3	K_4
CA-CA-CS-ST	7.2500	0.0000	-7.2500	0.0000	0.0000
CA-CA-CS-CS	7.2500	0.0000	-7.2500	0.0000	0.0000
CA-CS-ST-CS	7.2500	0.0000	-7.2500	0.0000	0.0000
CS-CS-ST-CS	7.2500	0.0000	-7.2500	0.0000	0.0000
CA-CS-CS-CA	0.1042	-0.0396	-0.7177	0.1355	-0.2130
CA-CS-CS-ST	0.1276	0.0000	-0.9179	0.0000	0.0000
ST-CS-CS-ST	0.1042	-0.0396	-0.7177	0.1355	-0.2130
CS-CA-CA-CS	7.2500	0.0000	-7.2500	0.0000	0.0000

S2.2 Coarse-grained force field parameter

A CG model in our previous study (68) was adopted to simulate 5T/dC6/EOn, where three types of CG beads were defined to discriminate the interaction strength between molecular segments. To develop this model, the bonded interactions were parameterized by reproducing the intramolecular bond and angle distributions from the reference atomistic simulations, and the nonbonded interactions were obtained by fitting the experimental saturated liquid densities in the vapor-liquid equilibrium of target molecules. For the CG representation of 5T/dC6/EOn shown in **Fig. S4**, each thiophene ring is modeled by a single type TH bead (69), and the alkyl and EOn segments are modeled by a chain of type AK and EO beads, respectively, based on a regular three-to-one scheme (70), where one CG bead contains three heavy atoms with their accompanying hydrogen atoms. For simplicity, a single EO bead representing four heavy atoms is used to accommodate the specific structure bridging 5T and EOn segments in 5T/dC6/EO4 and 5T/dC6/EO10.

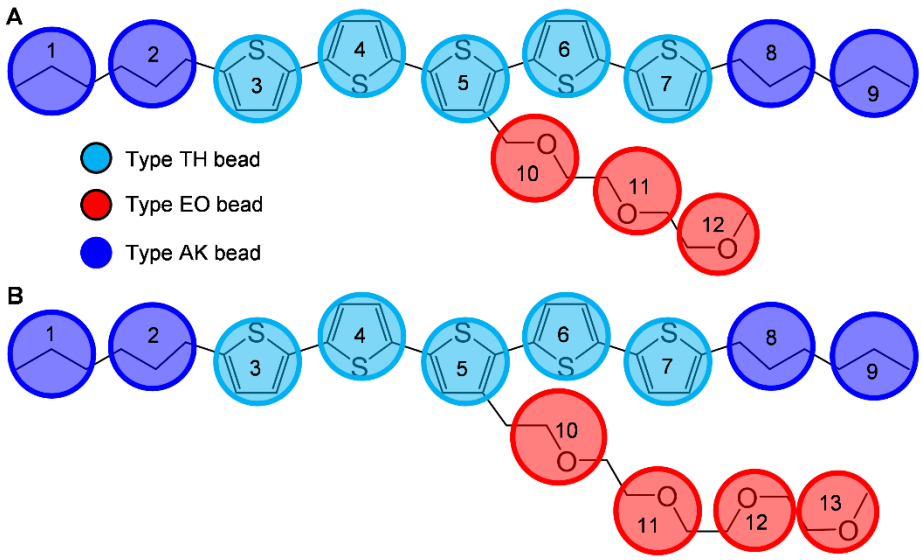

Fig. S4. Reference labels for bead types in the CG force field and related mapping scheme for 5T/dC6/EOn molecules. (A) 5T/dC6/EO3 and (B) 5T/dC6/EO4.

Nonbonded interactions between CG beads are described by the Lennard-Jones (LJ) potential with parameters listed in **Table S10**,

$$U_{\mathrm{CG-NB}} = 4\epsilon_{ij}\left[\left(\frac{\sigma_{ij}}{r_{ij}}\right)^{12} - \left(\frac{\sigma_{ij}}{r_{ij}}\right)^{6}\right] \tag{S7}$$

where r_{ij} is the distance between bead i and j, σ_{ij} is the van de Walls diameter and ϵ_{ij} is the well-depth parameter both defined by the bead types. All beads are neutral with modified masses to reflect their corresponding groups of atoms. To better capture the driving force of the self-assembly, a modified Lorentz-Berthelot mixing rule (71-73) is used for the cross-species LJ potentials in the CG model,

$$\sigma_{ij} = \frac{1}{2}\left(\sigma_{ii} + \sigma_{jj}\right) \quad , \quad \epsilon_{ij} = (1-\zeta)\sqrt{\epsilon_{ii}\epsilon_{jj}} \tag{S8}$$

For the cross-species energy parameter, ϵ_{ij}, a binary coefficient ζ is introduced to control the miscibility between different segments of 5T/dC6/EOn. The coefficient ζ was determined by fitting the corresponding radial distribution function (RDF) obtained from the AA simulation of binary mixtures (68). The cross-species LJ potentials with optimized coefficients ζ are summarized in **Table S11**. Bonded interactions among CG beads only include the bond stretching and angle bending interactions also described by the harmonic form in **Equation S3 and S4** with parameters listed in **Tables S12 and S13**. Note that the angle type, EO-TH-TH, refers to the bending angle formed by the following CG beads, 4-5-10, using their bead IDs illustrated in **Fig. S4A**. There is

no additional interaction for the bending angle formed by beads of 6-5-10. In addition, the nonbonded interactions are truncated and shifted to 0.0 at 12 Å, which are turned off only for atoms that are directly bonded.

Table S10. Nonbonded parameters for CG model of 5T/dC6/EOn.

CG bead type *i*	m / (g/mol)	σ_{ii} / Å	ϵ_{ii} / (kcal/mol)
TH	82.120	4.83	1.04
EO	44.053	4.28	0.50
AK	42.081	4.55	0.58

Table S11. Cross-species LJ potential parameters for CG model of 5T/dC9/EO3.

CG bead type *i*	CG bead type *j*	ζ	σ_{ij} / Å	ϵ_{ij} / (kcal/mol)
EO	TH	0.16	4.555	0.6057
AK	TH	0.14	4.690	0.6679
AK	EO	0.10	4.415	0.4847

Table S12. Harmonic bond stretching potential parameters for CG model of 5T/dC6/EOn.

bond	K_b / (kcal·mol^{-1}·Å^{-2})	r_0 / Å
AK-AK	8.735	3.68
AK-TH	17.709	3.75
TH-TH	89.012	3.89
EO-TH	13.512	3.88
EO-EO	5.286	3.25

Table S13. Harmonic angle bending potential parameters for CG model of 5T/dC6/EOn.

angle	K_θ / (kcal·mol^{-1}·rad^{-2})	θ_0 / °
AK-AK-TH	3.787	160
AK-TH-TH	5.757	168
TH-TH-TH	21.948	165
EO-TH-TH	12.766	127
EO-EO-TH	3.644	136
EO-EO-EO	2.187	145

S2.3 Simulation protocols for the self-assembly of 5T/dC6/EOn

Given the current hardware and computational budgets, the CG model was employed to study the self-assembly of 5T/dC6/EOn. The CG simulation was performed in the cubic simulation box with the periodic boundary conditions and was integrated by the velocity-Verlet algorithm with the integration step size of 1 fs. The Nośe-Hoover thermostat and barostat with a damping parameter of 100 fs and 1000 fs were used to maintain the constant temperature and pressure, respectively. To find ordered structures, a simple quench process was performed in the isothermal-isobaric ensemble (*NPT*) at 1 atm over a range of temperatures. The system was initially simulated at a relatively high temperature to reach a well-equilibrated isotropic state. The system was then cooled down stepwise by ΔT = 10 K over a period of 2 ns and equilibrated at this decreased temperature for another 20 ns, whose final configuration was used as input for the next quench step. After several quench steps, the system reached the lower temperature and often formed an ordered phase.

S2.4 Simulation protocols for the Li-ion transport in 5T/dC6/EOn

Since atomistic details are desired to study the Li-ion transport, the AA model was employed to simulate 5T/dC6/EOn and Li-ions. The AA simulation was performed in the periodic box and integrated by the velocity-Verlet algorithm with the integration step size of 1 fs. The Nośe-Hoover thermostat and barostat with a damping parameter of 100 fs and 1000 fs were used to maintain the constant temperature and pressure, respectively. Initial AA configurations of 5T/dC6/EOn were converted from well-equilibrated CG ones generated from the self-assembly simulations using the backmapping method (74-79). Li-ions were then randomly added into 5T/dC6/EOn at a ratio of $r = [Li^+]/[EO] = 0.05$. The mixture of Li-ions and 5T/dC6/EOn molecules was first equilibrated in the isothermal-isobaric ensemble (*NPT*) at the designated temperature and 1 atm for 5 ns, and further equilibrated in the canonical ensemble (*NVT*) at the same temperature for 5 ns using the average box size calculated from the last 4 ns of the *NPT* run. Taking the resulting equilibrated configuration as a starting structure, the Li-ion transport was then studied upon the application of an external electric field for good statistical sampling. A production run of 120 ns was performed in the *NVT* ensemble at the designated temperature with a unidirectional electric field of 0.5 V/nm along *x*-axis.

S3 Self-assembly of 5T/dC6/EOn in CG simulations

The self-assembly of 5T/dC6/EOn was simulated by the CG force field using a quenching process. At lower temperatures, 5T/dC6/EO3 and 5T/dC6/EO4 were found to form a lamellar phase, while 5T/dC6/EO10 were found to form a column phase. In these ordered structures, rigid 5T segments align roughly in the same direction. To measure the structural order of 5T segments, the nematic order parameter, P_2 (80) is calculated by

$$P_2 = \max_{\boldsymbol{n}} \frac{1}{N}\sum_{i=1}^{N}\left(\frac{3}{2}|\boldsymbol{u}_i \cdot \boldsymbol{n}|^2 - \frac{1}{2}\right) = \max \frac{1}{N}\sum_{i=1}^{N}\left(\frac{3}{2}\cos^2\varphi_i - \frac{1}{2}\right) \quad \text{(S9)}$$

where N is the number of molecules, $\boldsymbol{u}_i = (u_{i,x}, u_{i,y}, u_{i,z})$ is the end-to-end unit vector of the 5T segment, $\boldsymbol{n}$ is a unit vector ("director") for which P_2 is maximized, φ_i is the angle between $\boldsymbol{u}_i$ and $\boldsymbol{n}$. This nematic director, $\boldsymbol{n}$, can be found from the following second order tensor,

$$\boldsymbol{Q}_{mn} = \frac{1}{N}\sum_{i=1}^{N}\left(\frac{3}{2}u_{i,m}u_{i,n} - \frac{1}{2}\delta_{mn}\right), \quad m,n = x,y,z \quad \text{(S10)}$$

where δ_{mn} is the Kronecker delta function. The nematic director is the eigenvector associated with the largest eigenvalue of $\boldsymbol{Q}_{mn}$. P_2 takes on a value between 0 for a disordered phase and 1 for a nematic phase. Then, P_2 can be used to give an approximation of the transition temperature between the isotropic state and these ordered structures of 5T/dC6/EOn (**Fig. S5**).

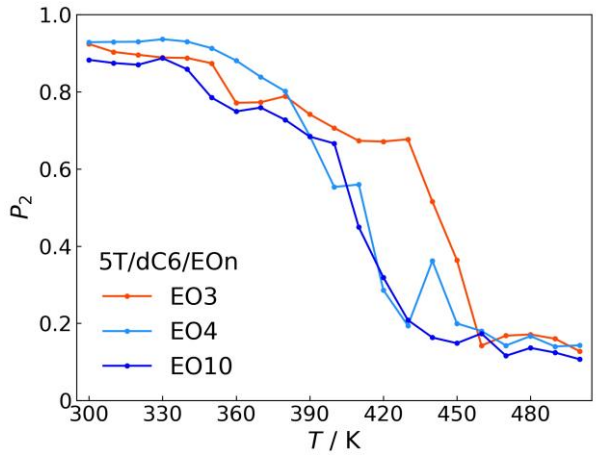

Fig. S5. Nematic order parameter as function of temperature for 5T/dC6/EOn in CG simulations.

To obtain the diffraction pattern from an AA configuration, the structure factor, $S(\boldsymbol{q})$, is calculated by

$$S(\boldsymbol{q}) = \left(\sum_j f_j(q)\cos(\boldsymbol{q}\cdot\boldsymbol{R}_j)\right)^2 + \left(\sum_j f_j(q)\sin(\boldsymbol{q}\cdot\boldsymbol{R}_j)\right)^2 \quad \text{(S11)}$$

where $\boldsymbol{q}$ is the scattering vector with a magnitude of q, $f_j(q)$ is the atomic form factor of atom j, and $\boldsymbol{R}_j$ is the position vectors of atom j. Due to the periodic boundaries, the scattering vector is restricted to integer numbers of wavelengths within the simulation box. For a cuboid simulation box we used, the box vectors in real space ($\boldsymbol{L}_x$, $\boldsymbol{L}_y$, $\boldsymbol{L}_z$) and in reciprocal space ($\boldsymbol{L}_x^*$, $\boldsymbol{L}_y^*$, $\boldsymbol{L}_z^*$) are given by

$$\begin{bmatrix}\boldsymbol{L}_x\\ \boldsymbol{L}_y\\ \boldsymbol{L}_z\end{bmatrix} = \begin{bmatrix}L_x & 0 & 0\\ 0 & L_y & 0\\ 0 & 0 & L_z\end{bmatrix} \quad \text{(S12)}$$

$$\begin{bmatrix}\boldsymbol{L}_x^*\\ \boldsymbol{L}_y^*\\ \boldsymbol{L}_z^*\end{bmatrix} = 2\pi\begin{bmatrix}1/L_x & 0 & 0\\ 0 & 1/L_y & 0\\ 0 & 0 & 1/L_z\end{bmatrix} \quad \text{(S13)}$$

where L_x, L_y and L_z are box lengths in the x-, y- and z-axis. Accordingly, the scattering vector can be constructed using three integer numbers (n_x, n_y, n_z) and the reciprocal box vectors,

$$\boldsymbol{q}_{nx,ny,nz} = n_x\boldsymbol{L}_x^* + n_y\boldsymbol{L}_y^* + n_z\boldsymbol{L}_z^* = 2\pi\left(\frac{n_x}{L_x}, \frac{n_y}{L_y}, \frac{n_z}{L_z}\right) \quad \text{(S14)}$$

Each scattering vector actually defines one specific periodic symmetry by constructing a set of parallel planes with the same normal vector of $\boldsymbol{q}_{nx,ny,nz}$ and the equal interplanar spacing of $d_{nx,ny,nz}$,

$$d_{nx,ny,nz} = \frac{2\pi}{|\boldsymbol{q}_{nx,ny,nz}|} \quad \text{(S15)}$$

In principle, given a scattering vector, atoms located exactly in the corresponding set of parallel planes will create constructive inference for X-rays, while atoms located in between these planes will generate different degrees of destructive inference with the largest degree being the atoms at the exact middle of two adjacent parallel planes. Despite different atomic form factors, the X-ray diffraction at a given scattering vector will have complete constructive interference with a strong intensity when all the atoms are placed in the corresponding set of planes, while the diffraction will have complete destructive interference with no intensity when half of the atoms are placed in the corresponding parallel planes and half located in the middle of any two adjacent parallel planes. Therefore, to connect atomistic packing details with the diffraction pattern, different sets of parallel planes related to diffraction peaks are drawn along with the AA configuration.

For the diffraction pattern shown in **Fig. 3A**, the set of parallel planes related to the peak at $q_r \approx 0.33$ Å^{-1} align well with the center of each EOn cluster (**Fig. S6A**), indicating the embedded periodic symmetry among these clusters, and the intermediate intensity is on account of the

destructive interference made by the rest 5T and alkyl segments. Moreover, parallel planes related to diffraction peaks between $q_r \approx 1.32$ Å^{-1} and $q_r \approx 1.39$ Å^{-1} show a good alignment with the longitudinal direction of 5T segments (**Fig. S6B–D**), making a considerable contribution to the constructive interference. Accordingly, by assigning proper Miller indices for these three diffraction peaks, the packing of 5T segments alone can be roughly represented by a 2D centered lattice with a parallelogrammatic unit cell.

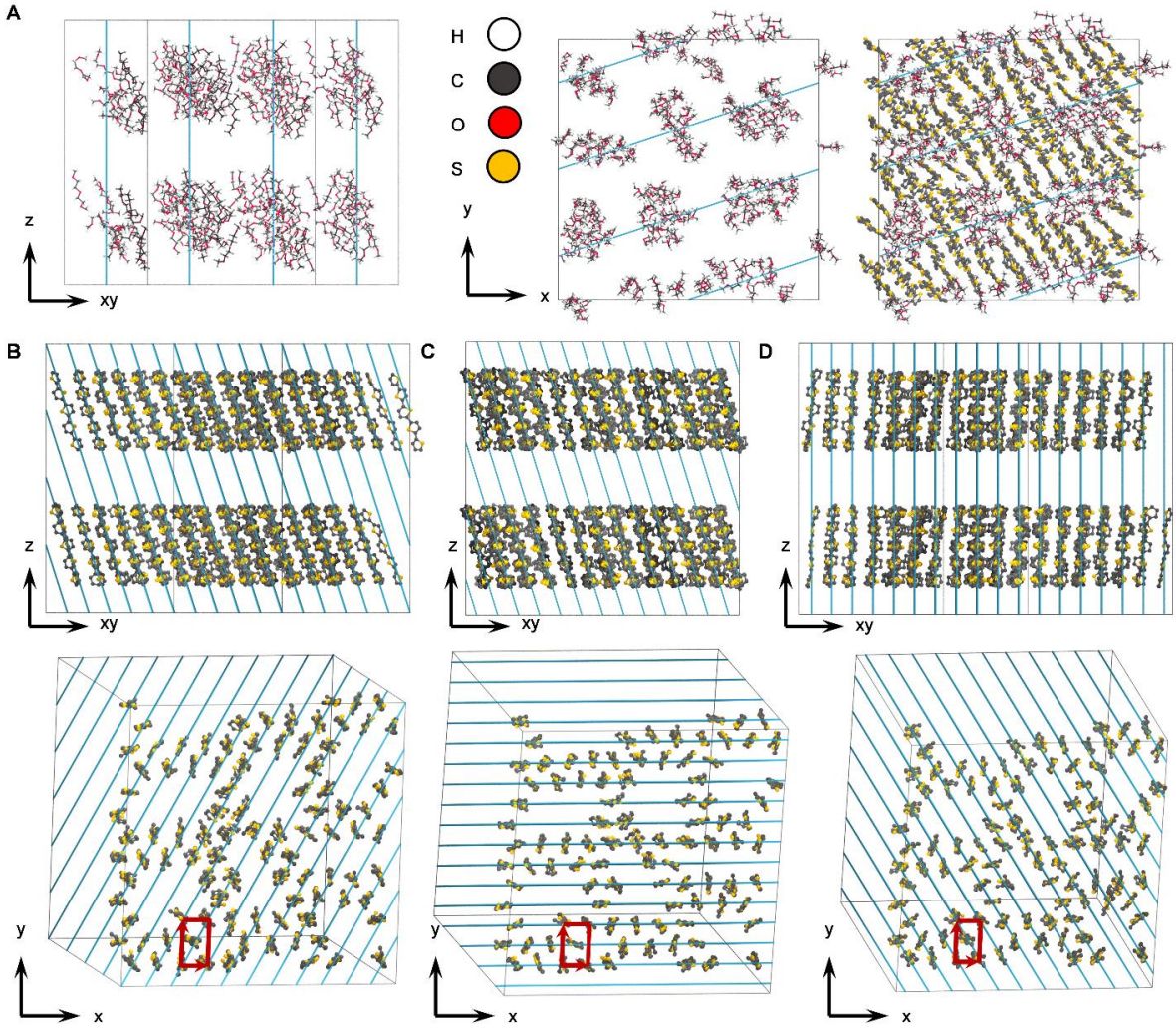

Fig. S6. Periodic symmetry of 5T/dC6/EO3 configuration. For clarity, only 5T and EO3 segments are shown. Groups of equally spaced parallel lines in blue represent different sets of parallel planes related to the scattering vector of (A) $q_r = 0.335$ Å^{-1}, (B) $q_r = 1.329$ Å^{-1}, (C) $q_r = 1.378$ Å^{-1} and (D) $q_r = 1.383$ Å^{-1}. In (B)–(D), the unit cell of 5T packing is drawn with red lines.

S4 Li-ion transport in 5T/dC6/EOn with AA simulations

S4.1 Mobility of Li-ions and oxygen atoms

A simulation trajectory can track all motions of Li-ions and 5T/dC6/EOn molecules. To better capture Li-ion migration, any drift motion of 5T/dC6/EOn molecules needs to be separated by subtracting the total center of mass (COM) of the host 5T/dC6/EOn molecules from atomic coordinates in each frame of a trajectory. Under the electric field, the charged Li-ion is expected to yield a linear response behavior (Ohm's law) (52), reaching the regime of MSD ~ t^2. Our simulation results at 300 K (**Fig. S7**) show that slopes of Li-ion MSDs on a log-log scale are less than unity after 60 ns due to the slow dynamics and isolated EO domains in the ordered structures (**Fig. 2**). Thus, long expensive simulations are required at low temperatures to observe important transport events, e.g., Li-ion hopping between EO segments. To provide necessary mechanistic insights of the Li-ion transport, our simulations were mainly performed at 400 K with disordered structures for better sampling.

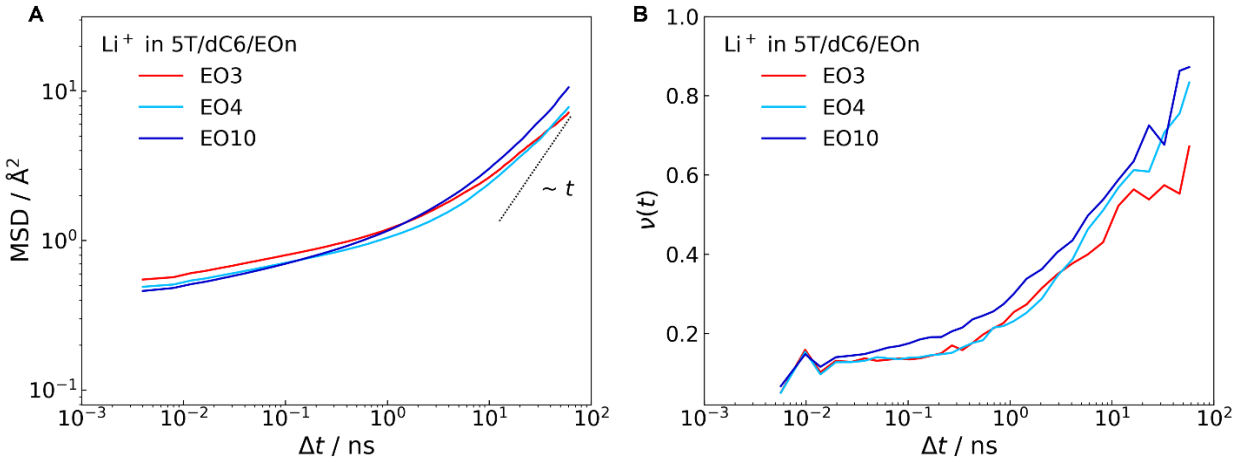

Fig. S7. Li-ion transport in 5T/dC6/EOn at 300 K. (A) MSD curves, (B) their apparent power-law exponents.

Dynamics of 5T/dC6/EOn was also studied at 400 K focusing on the mobility of oxygen atoms due to their strong interaction with Li-ions. Oxygen atoms move faster than Li-ions at intermediate times, which are expected to be surpassed by Li-ions at long times due to their smaller power-law exponents (**Fig. S8A–B**). Further comparisons are made on the apparent oxygen diffusivity evaluated at 60 ns for different chain positions with index-1 being the oxygen closest to 5T core (**Fig. S8C**). The increased mobility is observed for the oxygen close to the free end of

the EOn sidechain. 5T/dC6/EO4 exhibits the slowest oxygen mobility consistent with the Li-ion results. In 5T/dC6/EO3, faster oxygen mobilities for all three positions are likely related to smaller molecular shape with easier intermolecular motion. In 5T/dC6/EO10, faster oxygen mobilities close to the chain end are likely related to larger domains of flexible EO10 chains with more free volumes to explore.

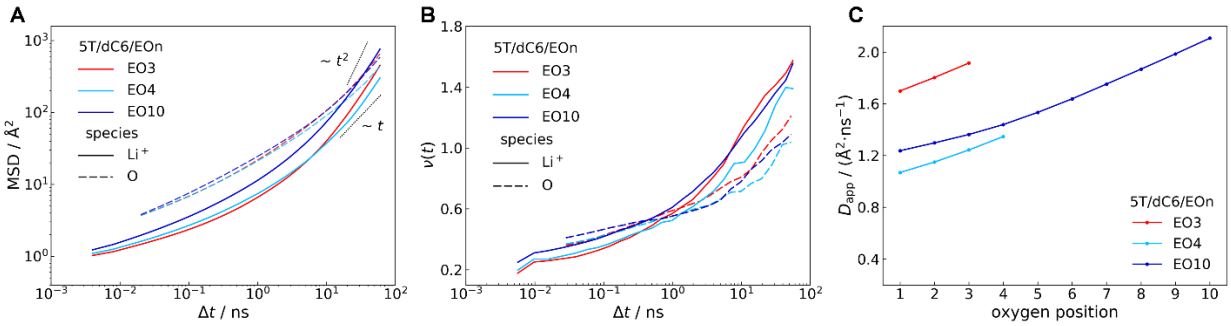

Fig. S8. Transport properties simulated at 400 K. (A) MSD and (B) apparent power-law exponent for Li-ions and oxygen atoms. Curves for Li-ion and oxygen are marked by full/dashed lines, respectively, and molecular systems given different colors. (C) Apparent oxygen diffusivity computed at 60 ns as a function of the position along the EOn segment.

S4.2 Li-ion solvation shell

The Li-ion solvation motif is denoted by the number of oxygen atoms, EOn segments and 5T/dC6/EOn molecules participating in the solvation shell. Interestingly, most observed motifs have the same number of segments and molecules, which is likely due to the steric constraint posed by short EOn segments in our studied molecules. However, one exceptional case of 6-2-1 is identified in 5T/dC6/EO10 with very low frequency, where a Li-ion is coordinated by six oxygen atoms from two noncontiguous segments but within the same molecule (**Fig. S9A**). Motifs with unequal number of segments and molecules are expected to exhibit greater prevalence as the length of EOn segment increases. In addition, oxygen atoms in the Li-ion solvation shell were classified based on their positions in the EOn segment with index-1 being the oxygen closest to 5T core (**Fig. S9B**). In 5T/dC6/EO3, oxygen atoms at different positions exhibit very similar probabilities to participate in the solvation shell, as every oxygen of a given segment is indispensable to form 6-2-2 motif. In 5T/dC6/EO4, three oxygen atoms with index 2–4 coordinate the Li-ion with roughly the same probability, while index-1 oxygen shows a much lower probability likely due to its stronger surrounding crowding from rigid 5T core. In 5T/dC6/EO10, a gradual trend of increasing

probability is observed along the EOn segment with decreasing crowding from 5T core, and the maximum probability occurs at index-8 where the oxygen exhibits adequate flexibility and a high statistical permutation to form the solvation shell (51, 81).

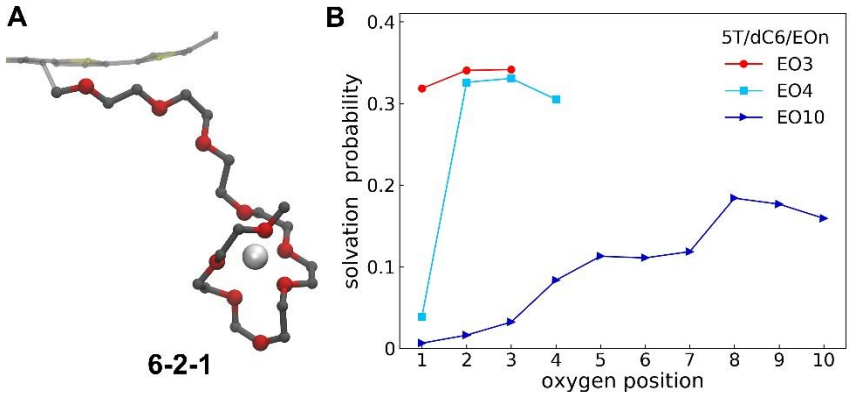

Fig. S9. Li-ion solvation shell. (A) Representative snapshot of 6-2-1 motif. Li-ions are colored in white, carbon atoms in gray, oxygen atoms in red, and sulfur atoms in yellow. For clarity, hydrogen atoms are omitted, and the 5T/dC6 backbones are cropped and shown partially transparent. (B) Solvation probability of oxygen atoms around Li-ions as a function of the position along the EOn segment.

Individual Li-ion solvation shell can be examined to provide some complementary details of direct hopping events. Given a Li-ion, changes in its solvation shell can be illustrated by tracking the indices of constituent oxygen atoms at different times in a simulation trajectory. A bar plot is used to mark the duration of specific oxygen atoms in the solvation shell, where some bars are intermittent due to the back-and-forth movement of a Li-ion along EOn segments. For clarity, oxygen atoms coordinating a Li-ion for a very brief period, less than half of a 0.4 ns interval, are excluded from this analysis as simulation fluctuations. For a specific Li-ion in 5T/dC6/EO3 (**Fig. S10**), interchain hopping usually changes half of oxygen atoms in the solvation shell, i.e., replacing one coordinating EO3 segment by a free one, and sometimes a three-chain motif was observed as the transition state for a short period. Similar interchain hopping events were observed in 5T/dC6/EO4 as well but with lower frequencies. For a certain Li-ion in 5T/dC6/EO10 (**Fig. S11**), intrachain hopping is very common across different motifs, where the Li-ion drifts along the EO10 segment. Interchain hopping often undergoes a two-chain motif, where one chain gradually leaves the solvation shell. Sometimes, a sudden jump from one chain to another was also observed in simulations.

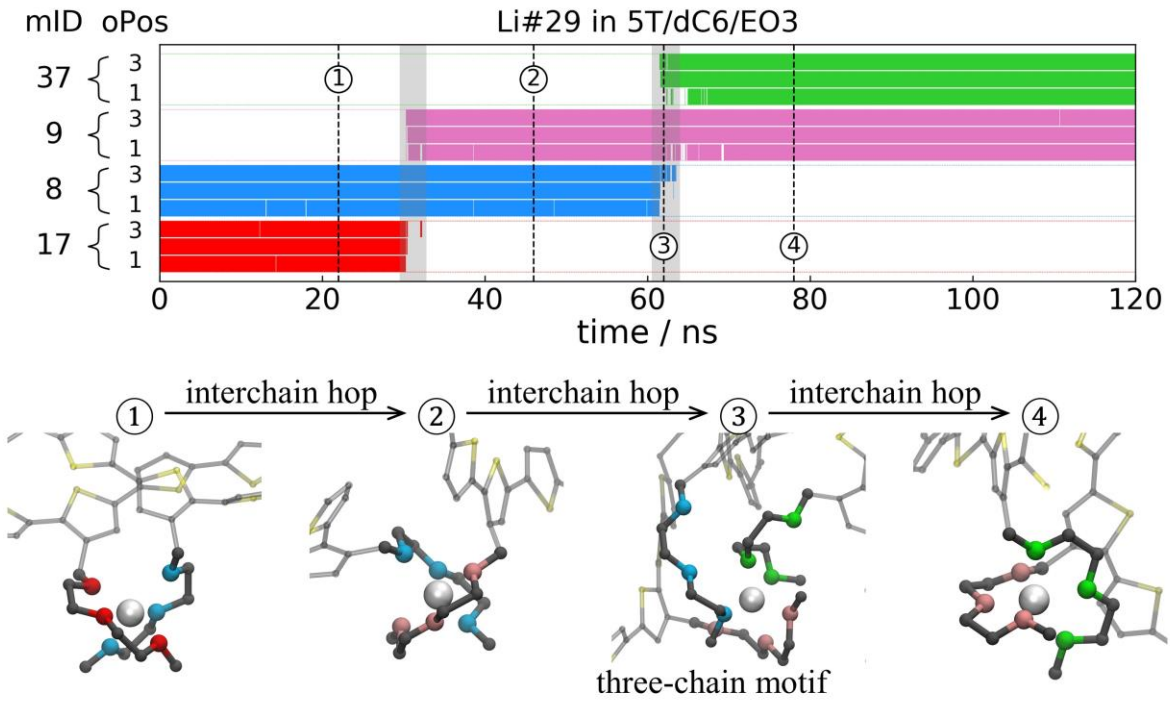

Fig. S10. Evolution of an individual Li-ion solvation shell in 5T/dC6/EO3. Oxygen atoms in the shell are drawn by bars to indicate their residence time, and a single color is used for oxygen atoms from the same molecule. Oxygen atoms are differentiated by their molecular index (mID) and the relative position (oPos) along the EOn segment with index-1 being the closest to 5T core. Snapshots at representative times marked by vertical lines in the bar plot are shown to illustrate the solvation shell before and after certain hopping events highlighted in gray shade to roughly indicate their durations. Li-ions are colored in white, carbon atoms in gray, and sulfur atoms in yellow. For illustration, oxygen atoms from different molecules are colored consistently with the bar plot. For clarity, hydrogen atoms are omitted, and 5T/dC6 backbones are cropped and shown partially transparent.

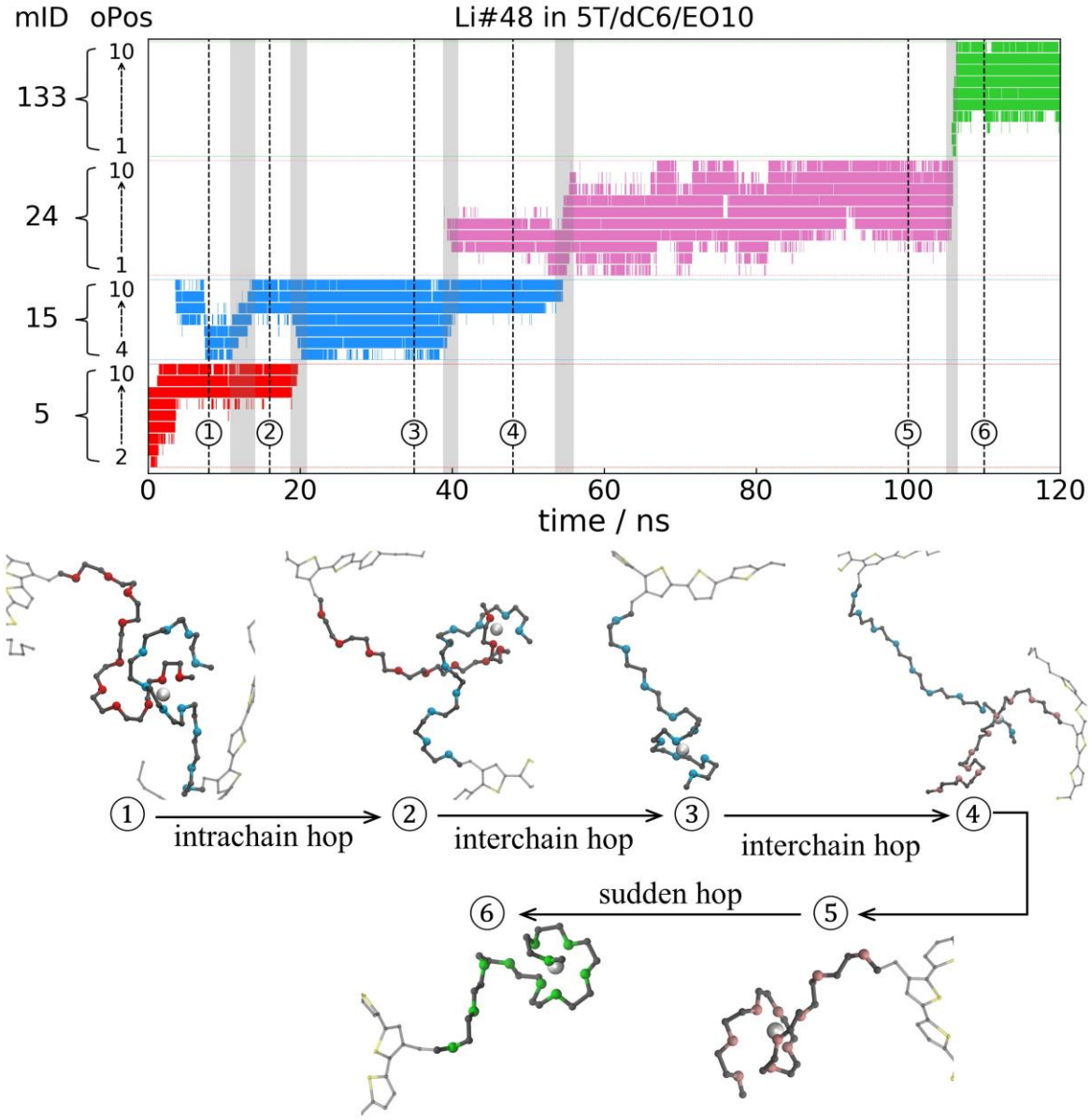

Fig. S11. Evolution of an individual Li-ion solvation shell in 5T/dC6/EO10.

S4.3 Solvation sites in ion-conducting EOn domains

Solvation site is defined as the centroid of a set of six or more oxygen atoms if each of which is also within a threshold distance of r_{site} = 3.4 Å around the centroid. In a simulated configuration, each oxygen atom is labeled consecutively with a unique index to form a set of $\{O_i\}$. In principle, the complete list of solvation sites in a configuration can be obtained by enumerating all the combinations of six or more atoms from $\{O_i\}$ while determining whether they satisfy the definition of solvation site. In practice, for algorithm efficiency, some necessary conditions are used to quickly eliminate invalid atom combinations. It is readily to see that the maximum distance between two oxygen atoms to form a solvation site is twice the threshold distance, $2r_{site}$, where the solvation site is placed exactly at the middle of two atoms. Given an oxygen atom referred as "center", O_i, its neighbor list is built containing all the other oxygen atoms within $2r_{site}$,

$$O_i(\text{neighbor}) = \left\{O_{j\neq i}\text{ , if } r_{ij} \leq 2r_{\text{site}}\right\} \tag{S16}$$

where r_{ij} is the distance between atom O_i and O_j. Apparently, solvation sites can only be formed by combinations of "center" atom with its neighbor atoms. For each oxygen atom, enumerate all the six-or-more-atom combinations using itself and its neighbor list, and examine their validity for the solvation site. To illustrate the validity check, take a general proposed six-atom combination as an example, "O_i+O_{j1}-O_{j2}-O_{j3}-O_{j4}-O_{j5}", where O_i is the center oxygen atom and O_{j1} to O_{j5} are five oxygen atoms in its neighbor list. A quick screening is initially performed to only select combinations satisfying that each atom is also in the neighbor lists of the rest five atoms, e.g., O_{j1} in O_{j2}(neighbor), O_{j1} in O_{j3}(neighbor) and so on. Then, for these selected combinations, the centroid of six atoms is calculated along with the atom-centroid distances to finally determine whether they satisfy the definition of solvation site. When all valid solvation sites are found, an additional check confirms that the oxygen-atom-combination of any solvation site is not a subset of the atom-combination associated with another site, such that each site corresponds to a unique list of atoms.

According to the radial autocorrelation function of solvation site for "unique" atoms (RACF-ST_{unique}) in **Equation 6**, any site within a distance from the reference site is examined, and the one giving the maximum value is selected. To better understand this parameter, **Fig. S12** shows RACF-ST of some individual reference sites, and these plots only change values at the distance where new neighboring sites are included, leading to a stepwise shape.

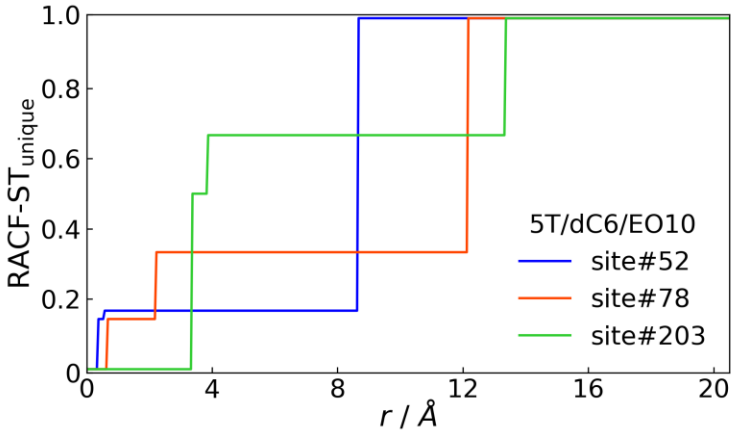

Fig. S12. Illustration of radial autocorrelation function (RACF-ST) using individual solvation sites in 5T/dC6/EO10.

REFERENCES AND NOTES

1. S. Allard, M. Forster, B. Souharce, H. Thiem, U. Scherf, Organic semiconductors for solution-processable field-effect transistors (OFETs). *Angew. Chem. Int. Ed. Engl.* **47**, 4070–4098 (2008).

2. S. Sergeyev, W. Pisula, Y. H. Geerts, Discotic liquid crystals: A new generation of organic semiconductors. *Chem. Soc. Rev.* **36**, 1902–1929 (2007).

3. F. Huang, H. Wu, Y. Cao, Water/alcohol soluble conjugated polymers as highly efficient electron transporting/injection layer in optoelectronic devices. *Chem. Soc. Rev.* **39**, 2500–2521 (2010).

4. M. Funahashi, Development of liquid-crystalline semiconductors with high carrier mobilities and their application to thin-film transistors. *Polym. J.* **41**, 459–469 (2009).

5. W. Pisula, M. Zorn, J. Y. Chang, K. Müllen, R. Zentel, Liquid crystalline ordering and charge transport in semiconducting materials. *Macromol. Rapid Commun.* **30**, 1179–1202 (2009).

6. L. Schmidt-Mende, A. Fechtenkötter, K. Müllen, E. Moons, R. H. Friend, J. D. MacKenzie, Self-organized discotic liquid crystals for high-efficiency organic photovoltaics. *Science* **293**, 1119–1122 (2001).

7. T. Hori, Y. Miyake, N. Yamasaki, H. Yoshida, A. Fujii, Y. Shimizu, M. Ozaki, Solution processable organic solar cell based on bulk heterojunction utilizing phthalocyanine derivative. *Appl. Phys. Express* **3**, 101602 (2010).

8. W. Shin, T. Yasuda, G. Watanabe, Y. S. Yang, C. Adachi, Self-organizing mesomorphic diketopyrrolopyrrole derivatives for efficient solution-processed organic solar cells. *Chem. Mater.* **25**, 2549–2556 (2013).

9. A. Seki, K. Shimizu, K. Aoki, Chiral π-conjugated liquid crystals: Impacts of ethynyl linker and bilateral symmetry on the molecular packing and functions. *Crystals* **12**, 1278 (2022).

10. A. E. A. Contoret, S. R. Farrar, P. O. Jackson, S. M. Khan, L. May, M. O'Neill, J. E. Nicholls, S. M. Kelly, G. J. Richards, Polarized electroluminescence from an anisotropic nematic network on a non-contact photoalignment layer. *Adv. Mater.* **12**, 971–974 (2000).

11. T. Hassheider, S. A. Benning, H. S. Kitzerow, M. F. Achard, H. Bock, Color-tuned electroluminescence from columnar liquid crystalline alkyl arenecarboxylates. *Angew. Chem. Int. Ed. Engl.* **40**, 2060–2063 (2001).

12. S. A. Benning, R. Oesterhaus, H. Kitzerow, Polarized electroluminescence of a discotic mesogenic compound. *Liq. Cryst.* **31**, 201–205 (2004).

13. M. P. Aldred, A. E. A. Contoret, S. R. Farrar, S. M. Kelly, D. Mathieson, M. O'Neill, W. C. Tsoi, P. Vlachos, A full-color electroluminescent device and patterned photoalignment using light-emitting liquid crystals. *Adv. Mater.* **17**, 1368–1372 (2005).

14. A. J. J. M. van Breemen, P. T. Herwig, C. H. T. Chlon, J. Sweelssen, H. F. M. Schoo, S. Setayesh, W. M. Hardeman, C. A. Martin, D. M. de Leeuw, J. J. P. Valeton, C. W. M. Bastiaansen, D. J. Broer, A. R. Popa-Merticaru, S. C. J. Meskers, Large area liquid crystal monodomain field-effect transistors. *J. Am. Chem. Soc.* **128**, 2336–2345 (2006).

15. M. Funahashi, F. Zhang, N. Tamaoki, High ambipolar mobility in a highly ordered smectic phase of a dialkylphenylterthiophene derivative that can be applied to solution-processed organic field-effect transistors. *Adv. Mater.* **19**, 353–358 (2007).

16. Y. Shimizu, K. Oikawa, K. Nakayama, D. Guillon, Mesophase semiconductors in field effect transistors. *J. Mater. Chem.* **17**, 4223–4229 (2007).

17. W. Pisula, A. Menon, M. Stepputat, I. Lieberwirth, U. Kolb, A. Tracz, H. Sirringhaus, T. Pakula, K. Müllen, A zone-casting technique for device fabrication of field-effect transistors based on discotic hexa-*peri*-hexabenzocoronene. *Adv. Mater.* **17**, 684–689 (2005).

18. J. C. Maunoury, J. R. Howse, N. L. Turner, Melt-processing of conjugated liquid crystals: A simple route to fabricate OFETs. *Adv. Mater.* **19**, 805–809 (2007).

19. H. Monobe, K. Awazu, Y. Shimizu, Change of liquid-crystal domains by vibrational excitation for a columnar mesophase. *Adv. Mater.* **12**, 1495–1499 (2000).

20. A. Tracz, J. K. Jeszka, M. D. Watson, W. Pisula, K. Müllen, T. Pakula, Uniaxial alignment of the columnar super-structure of a hexa (alkyl) hexa-*peri*-hexabenzocoronene on untreated glass by simple solution processing. *J. Am. Chem. Soc.* **125**, 1682–1683 (2003).

21. V. De Cupere, J. Tant, P. Viville, R. Lazzaroni, W. Osikowicz, W. R. Salaneck, Y. H. Geerts, Effect of interfaces on the alignment of a discotic liquid−crystalline phthalocyanine. *Langmuir* **22**, 7798–7806 (2006).

22. Y. Sagara, T. Kato, Mechanically induced luminescence changes in molecular assemblies. *Nat. Chem.* **1**, 605–610 (2009).

23. T. Kato, M. Yoshio, T. Ichikawa, B. Soberats, H. Ohno, M. Funahashi, Transport of ions and electrons in nanostructured liquid crystals. *Nat. Rev. Mater.* **2**, 17001 (2017).

24. S. Yazaki, M. Funahashi, J. Kagimoto, H. Ohno, T. Kato, Nanostructured liquid crystals combining ionic and electronic functions. *J. Am. Chem. Soc.* **132**, 7702–7708 (2010).

25. B. D. Paulsen, K. Tybrandt, E. Stavrinidou, J. Rivnay, Organic mixed ionic–electronic conductors. *Nat. Mater.* **19**, 13–26 (2020).

26. Z. Liu, B. X. Dong, M. Misra, Y. Sun, J. Strzalka, S. N. Patel, F. A. Escobedo, P. F. Nealey, C. K. Ober, Self-assembly behavior of an oligothiophene-based conjugated liquid crystal and its implication for ionic conductivity characteristics. *Adv. Funct. Mater.* **29**, 1805220 (2019).

27. B. X. Dong, Z. Liu, M. Misra, J. Strzalka, J. Niklas, O. G. Poluektov, F. A. Escobedo, C. K. Ober, P. F. Nealey, S. N. Patel, Structure control of a π-conjugated oligothiophene-based liquid crystal for enhanced mixed ion/electron transport characteristics. *ACS Nano* **13**, 7665–7675 (2019).

28. Z. Wang, C. Wang, Y. Sun, K. Wang, J. W. Strzalka, S. N. Patel, P. F. Nealey, C. K. Ober, F. A. Escobedo, Ion transport in 2D nanostructured π-conjugated thieno[3,2-*b*]thiophene-based liquid crystal. *ACS Nano* **16**, 20714–20729 (2022).

29. W. H. Meyer, Polymer electrolytes for lithium-ion batteries. *Adv. Mater.* **10**, 439–448 (1998).

30. H. Wu, C. D. Wick, Computational investigation on the role of plasticizers on ion conductivity in poly(ethylene oxide) LiTFSI electrolytes. *Macromolecules* **43**, 3502–3510 (2010).

31. O. Borodin, G. D. Smith, Mechanism of ion transport in amorphous poly(ethylene oxide)/litfsi from molecular dynamics simulations. *Macromolecules* **39**, 1620–1629 (2006).

32. M. Funahashi, J. Hanna, High ambipolar carrier mobility in self-organizing terthiophene derivative. *Appl. Phys. Lett.* **76**, 2574–2576 (2000).

33. K. L. Woon, M. P. Aldred, P. Vlachos, G. H. Mehl, T. Stirner, S. M. Kelly, M. O'Neill, Electronic charge transport in extended nematic liquid crystals. *Chem. Mater.* **18**, 2311–2317 (2006).

34. S. Yazaki, M. Funahashi, T. Kato, An electrochromic nanostructured liquid crystal consisting of π-conjugated and ionic moieties. *J. Am. Chem. Soc.* **130**, 13206–13207 (2008).

35. V. Percec, M. Glodde, T. K. Bera, Y. Miura, I. Shiyanovskaya, K. D. Singer, V. S. K. Balagurusamy, P. A. Heiney, I. Schnell, A. Rapp, H. W. Spiess, S. D. Hudson, H. Duan, Self-organization of supramolecular helical dendrimers into complex electronic materials. *Nature* **419**, 384–387 (2002).

36. T. Yasuda, T. Shimizu, F. Liu, G. Ungar, T. Kato. Electro-functional octupolar π-conjugated columnar liquid crystals. *J. Am. Chem. Soc.* **133**, 13437–13444 (2011).

37. T. Ichikawa, M. Yoshio, A. Hamasaki, T. Mukai, H. Ohno, T. Kato, Self-organization of room-temperature ionic liquids exhibiting liquid-crystalline bicontinuous cubic phases: Formation of nano-ion channel networks. *J. Am. Chem. Soc.* **129**, 10662–10663 (2007).

38. T. Ichikawa, M. Yoshio, A. Hamasaki, S. Taguchi, F. Liu, X. Zeng, G. Ungar, H. Ohno, T. Kato, Induction of thermotropic bicontinuous cubic phases in liquid-crystalline ammonium and phosphonium salts. *J. Am. Chem. Soc.* **134**, 2634–2643 (2012).

39. T. Kato, N. Mizoshita, K. Kishimoto, Functional liquid-crystalline assemblies: Self-organized soft materials. *Angew. Chem. Int. Ed. Engl.* **45**, 38–68 (2006).

40. C. Tschierske, Development of structural complexity by liquid-crystal self-assembly. *Angew. Chem. Int. Ed. Engl.* **52**, 8828–8878 (2013).

41. Y. Sun, P. Padmanabhan, M. Misra, F. A. Escobedo, Molecular dynamics simulation of thermotropic bolaamphiphiles with a swallow-tail lateral chain: Formation of cubic network phases. *Soft Matter* **13**, 8542–8555 (2017).

42. Y. Sun, F. A. Escobedo, Coarse-grained molecular simulation of bolapolyphiles with a multident lateral chain: Formation and structural analysis of cubic network phases. *J. Chem. Theory Comput.* **20**, 1519–1537 (2024).

43. Z. Xue, D. He, X. Xie, Poly(ethylene oxide)-based electrolytes for lithium-ion batteries. *J. Mater. Chem. A* **3**, 19218–19253 (2015).

44. M. Misra, Z. Liu, B. X. Dong, S. N. Patel, P. F. Nealey, C. K. Ober, F. A. Escobedo, Thermal stability of π-conjugated n-ethylene-glycol-terminated quaterthiophene oligomers: A computational and experimental study. *ACS Macro Lett.* **9**, 295–300 (2020).

45. P. K. Lo, D. Chen, Q. Meng, M. S. Wong, Highly ordered smectic phases from polar calix[4]arene derivatives. *Chem. Mater.* **18**, 3924–3930 (2006).

46. W. Chen, B. Wunderlich, Nanophase separation of small and large molecules. *Macromol. Chem. Phys.* **200**, 283–311 (1999).

47. D. K. Paul, R. McCreery, K. Karan, Proton transport property in supported nafion nanothin films by electrochemical impedance spectroscopy. *J. Electrochem. Soc.* **161**, F1395–F1402 (2014).

48. C. G. Arges, Y. Kambe, H. S. Suh, L. E. Ocola, P. F. Nealey, Perpendicularly aligned, anion conducting nanochannels in block copolymer electrolyte films. *Chem. Mater.* **28**, 1377–1389 (2016).

49. H. Shimura, M. Yoshio, A. Hamasaki, T. Mukai, H. Ohno, T. Kato, Electric-field-responsive lithium-ion conductors of propylenecarbonate-based columnar liquid crystals. *Adv. Mater.* **21**, 1591–1594 (2009).

50. A. Eisele, K. Kyriakos, R. Bhandary, M. Schönhoff, C. M. Papadakis, B. Rieger, Structure and ionic conductivity of liquid crystals having propylene carbonate units. *J. Mater. Chem. A* **3**, 2942–2953 (2015).

51. D. Deng, M. A. Webb, P. Bennington, D. Sharon, P. F. Nealey, S. N. Patel, J. J. de Pablo, Role of molecular architecture on ion transport in ethylene oxide-based polymer electrolytes. *Macromolecules* **54**, 2266–2276 (2021).

52. B. X. Dong, C. Nowak, J. W. Onorato, J. Strzalka, F. A. Escobedo, C. K. Luscombe, P. F. Nealey, S. N. Patel, Influence of side-chain chemistry on structure and ionic conduction characteristics of polythiophene derivatives: A computational and experimental study. *Chem. Mater.* **31**, 1418–1429 (2019).

53. W. Chu, M. A. Webb, C. Deng, Y. J. Colón, Y. Kambe, S. Krishnan, P. F. Nealey, J. J. de Pablo, Understanding ion mobility in P2VP/NMP^{+}I^{-} polymer electrolytes: A combined simulation and experimental study. *Macromolecules* **53**, 2783–2792 (2020).

54. M. A. Webb, U. Yamamoto, B. M. Savoie, Z. G. Wang, T. F. Miller III, Globally suppressed dynamics in ion-doped polymers. *ACS Macro Lett.* **7**, 734–738 (2018).

55. M. A. Webb, Y. Jung, D. M. Pesko, B. M. Savoie, U. Yamamoto, G. W. Coates, N. P. Balsara, Z. G. Wang, T. F. Miller III, Systematic computational and experimental investigation of lithium-ion transport mechanisms in polyester-based polymer electrolytes. *ACS Cent. Sci.* **1**, 198–205 (2015).

56. M. A. Webb, B. M. Savoie, Z. G. Wang, T. F. Miller III, Chemically specific dynamic bond percolation model for ion transport in polymer electrolytes. *Macromolecules* **48**, 7346–7358 (2015).

57. D. M. Pesko, M. A. Webb, Y. Jung, Q. Zheng, T. F. Miller III, G. W. Coates, N. P. Balsara, Universal relationship between conductivity and solvation-site connectivity in ether-based polymer electrolytes. *Macromolecules* **49**, 5244–5255 (2016).

58. S. Yan, Y. Lu, F. Liu, Y. Xia, Q. Li, K. Liu, Zwitterionic matrix with highly delocalized anionic structure as an efficient lithium ion conductor. *CCS Chem.* **5**, 1612–1622 (2023).

59. W. L. Jorgensen, D. S. Maxwell, J. Tirado-Rives, Development and testing of the OPLS all-atom force field on conformational energetics and properties of organic liquids. *J. Am. Chem. Soc.* **118**, 11225–11236 (1996).

60. S. Plimpton, Fast parallel algorithms for short-range molecular dynamics. *J. Comput. Phys.* **117**, 1–19 (1995).

61. A. P. Thompson, H. M. Aktulga, R. Berger, D. S. Bolintineanu, W. M. Brown, P. S. Crozier, P. J. In't Veld, A. Kohlmeyer, S. G. Moore, T. D. Nguyen, R. Shan, M. J. Stevens, J. Tranchida, C. Trott, S. J. Plimpton, LAMMPS - A flexible simulation tool for particle-based materials modeling at the atomic, meso, and continuum scales. *Comp. Phys. Commun.* **271**, 10817 (2022).

62. W. M. Brown, P. Wang, S. J. Plimpton, A. N. Tharrington, Implementing molecular dynamics on hybrid high performance computers – short range forces. *Comput. Phys. Commun.* **182**, 898–911 (2011).

63. W. M. Brown, A. Kohlmeyer, S. J. Plimpton, A. N. Tharrington, Implementing molecular dynamics on hybrid high performance computers – Particle–particle particle-mesh. *Comput. Phys. Commun.* **183**, 449–459 (2012).

64. W. Humphrey, A. Dalke, K. Schulten, VMD: Visual molecular dynamics. *J. Mol. Graphics* **14**, 33–38 (1996).

65. D. Sharon, P. Bennington, C. Liu, Y. Kambe, B. X. Dong, V. X. Burnett, M. Dolejsi, G. Grocke, S. N. Patel, P. F. Nealey, Interrogation of electrochemical properties of polymer electrolyte thin films with interdigitated electrodes. *J. Electrochem. Soc.* **165**, H1028–H1039 (2018).

66. Z. Jiang, GIXSGUI: A MATLAB toolbox for grazing-incidence X-ray scattering data visualization and reduction, and indexing of buried three-dimensional periodic nanostructured films. *J. Appl. Cryst.* **48**, 917–926 (2015).

67. B. X. Dong, J. Strzalka, Z. Jiang, H. Li, G. E. Stein, P. F. Green, Crystallization mechanism and charge carrier transport in MAPLE-deposited conjugated polymer thin films. *ACS Appl. Mater. Interfaces* **9**, 44799–44810 (2017).

68. Y. Sun, "Computational study of self-assembly of amphiphilic and polyphilic molecules and application in li-ion transport," thesis, Cornell University, Ithaca, NY (2023).

69. H. S. Marsh, E. Jankowski, A. Jayaraman, Controlling the morphology of model conjugated thiophene oligomers through alkyl side chain length, placement, and interactions. *Macromolecules* **47**, 2736–2747 (2014).

70. H. Lee, A. H. de Vries, S. J. Marrink, R. W. Pastor, A coarse-grained model for polyethylene oxide and polyethylene glycol: Conformation and hydrodynamics. *J. Phys. Chem. B* **113**, 13186–13194 (2009).

71. Q. Du, Z. Yang, N. Yang, X. Yang, Coarse-grained model for perfluorocarbons and phase equilibrium simulation of perfluorocarbons/CO_2 mixtures. *Ind. Eng. Chem. Res.* **49**, 8271–8278 (2010).

72. P. Virnau, M. Müller, L. G. MacDowell, K. Binder, Phase behavior of *n*-alkanes in supercritical solution: A Monte Carlo study. *J. Chem. Phys.* **121**, 2169–2179 (2004).

73. F. A. Escobedo, Z. Chen, Liquid crystalline behavior of a semifluorinated oligomer. *J. Chem. Phys.* **121**, 11463–11473 (2004).

74. A. J. Rzepiela, L. V. Schäfer, N. Goga, H. J. Risselada, A. H. De Vries, S. J. Marrink, Reconstruction of atomistic details from coarse-grained structures. *J. Comput. Chem.* **31**, 1333–1343 (2010).

75. T. A. Wassenaar, K. Pluhackova, R. A. Böckmann, S. J. Marrink, D. P. Tieleman, Going backward: A flexible geometric approach to reverse transformation from coarse grained to atomistic models. *J. Chem. Theory Comput.* **10**, 676–690 (2014).

76. L. E. Lombardi, M. A. Martí, L. Capece, CG2AA: Backmapping protein coarse-grained structures. *Bioinformatics* **32**, 1235–1237 (2016).

77. J. Krajniak, S. Pandiyan, E. Nies, G. Samaey, Generic adaptive resolution method for reverse mapping of polymers from coarse-grained to atomistic descriptions. *J. Chem. Theory Comput.* **12**, 5549–5562 (2016).

78. J. Peng, C. Yuan, R. Ma, Z. Zhang, Backmapping from multiresolution coarse-grained models to atomic structures of large biomolecules by restrained molecular dynamics simulations using bayesian inference. *J. Chem. Theory Comput.* **15**, 3344–3353 (2019).

79. W. Li, C. Burkhart, P. Polińska, V. Harmandaris, M. Doxastakis, Backmapping coarse-grained macromolecules: An efficient and versatile machine learning approach. *J. Chem. Phys.* **153**, 041101 (2020).

80. B. S. John, C. Juhlin, F. A. Escobedo, Phase behavior of colloidal hard perfect tetragonal parallelepipeds. *J. Chem. Phys.* **128**, 044909 (2008).

81. P. Bennington, C. Deng, D. Sharon, M. A. Webb, J. J. de Pablo, P. F. Nealey, S. N. Patel, Role of solvation site segmental dynamics on ion transport in ethylene-oxide based side-chain polymer electrolytes. *J. Mater. Chem. A* **9**, 9937–9951 (2021).